

Illuminating Black Hole Shadow with Dark Matter Annihilation

Yifan Chen,¹ Ran Ding,² Yuxin Liu,^{3,4,5} Yosuke Mizuno,^{6,7} Jing Shu,^{8,9} Haiyue Yu,^{8,9} and Yanjie Zeng^{10,11}

¹*Niels Bohr International Academy, Niels Bohr Institute, Blegdamsvej 17, 2100 Copenhagen, Denmark*

²*School of Physics and Optoelectronics Engineering, Anhui University, Hefei 230601, China*

³*University of Chinese Academy of Sciences, Beijing 100190, China*

⁴*International Center for Theoretical Physics Asia-Pacific, Beijing/Hangzhou, China*

⁵*Department of Physics and Astronomy, University of Utah, Salt Lake City, Utah 84112, USA*

⁶*Tsung-Dao Lee Institute, Shanghai Jiao Tong University, 201210, Shanghai, China*

⁷*School of Physics & Astronomy, Shanghai Jiao-Tong University, 200240, Shanghai, China*

⁸*School of Physics and State Key Laboratory of Nuclear Physics and Technology, Peking University, Beijing 100871, China*

⁹*Center for High Energy Physics, Peking University, Beijing 100871, China*

¹⁰*CAS Key Laboratory of Theoretical Physics, Institute of Theoretical Physics,
Chinese Academy of Sciences, Beijing 100190, China*

¹¹*School of Physical Sciences, University of Chinese Academy of Sciences, Beijing 100049, China*

(Dated: May 3, 2024)

The Event Horizon Telescope (EHT) has revolutionized our ability to study black holes by providing unprecedented spatial resolution and unveiling horizon-scale details. With advancements leading to the next-generation EHT, there is potential to probe even deeper into the black hole's dark region, especially the inner shadow characterized by low-intensity foreground emissions from the jet, thanks to a significant enhancement in dynamic range by two orders of magnitude. We demonstrate how such enhanced observations could transform supermassive black holes into powerful probes for detecting annihilating dark matter, which can form a dense profile in the vicinity of supermassive black holes, by examining the morphology of the black hole image.

I. Introduction

The rapid development of the Very Long Baseline Interferometry (VLBI) technique has enabled extraordinarily high angular resolution in radio astronomy. A notable illustration of this progress is the recent imaging of supermassive black holes (SMBHs) achieved by the Event Horizon Telescope (EHT) [1, 2], which unveiled detailed astrophysical information in the strong gravity regions. Anticipated upgrades, like the next-generation EHT (ngEHT), promise further enhancements in angular resolution, dynamic range, and baseline coverage [3]. These advancements are pivotal not only for astrophysical insights but also for exploring fundamental physics, including testing general relativity, examining black hole (BH) properties, and investigating ultralight new bosons [4].

Beyond ultralight bosons, another class of potential new particles, often considered as dark matter (DM) candidates, exists around the GeV mass scale. These include weakly interacting massive particles [5] and sub-GeV DM [6]. In regions dominated by SMBHs' gravitational potential, the distribution of particle-like DM can steeply concentrate towards the BH, resulting in densities significantly higher than those near Earth [7]. Thus, SMBHs could serve as effective detectors for DM particles.

A promising approach for observing the DM spike is through indirect detection methods, like observing photons or cosmic rays resulting from potential DM annihilation [7]. These methods leverage the principle that the annihilation rate, directly proportional to the square of the density, increases significantly in regions of high den-

sity, thereby enhancing the production of particles. At the EHT's millimeter radio band, photons are typically produced via synchrotron radiation, where electrons spiral around magnetic field lines [8]. Understanding the magnetic field structure near the horizon is essential for predicting radio fluxes from DM annihilation. In this study, we employ the best-fit general relativistic magnetohydrodynamic (GRMHD) simulation, which aligns with EHT's observations of SMBH M87* [9, 10], specifically the magnetically arrested disk (MAD) model [11], to calculate the spectrum of DM annihilated electron-positron pairs near the SMBH and their resulting synchrotron radiation. Our results indicate that the density distribution of these pairs is similar in both equatorial and polar regions, contrasting with the MAD model prediction where electrons predominantly inhabit the disk, with lower densities in the jet region. Therefore, we propose utilizing the morphology of BH images, especially future observations of the inner shadow [12]—a region delineated by the lensed image of the equatorial horizon—to impose constraints on DM annihilation. These constraints appear significantly more stringent than those derived from the total intensity of the image [13, 14].

II. Electron-Positron Spectrum from Dark Matter Annihilations Near Supermassive Black Holes

The density of DM within a galaxy is typically highest at its center, and the presence of an SMBH can further sharpen this distribution, leading to an increased density towards the center. When considering an initial DM distribution profile where the mass of the central

SMBH is sufficiently low to influence the distribution, the slow accretion of ordinary matter onto the SMBH can lead to an adiabatic distortion of DM phase space by the SMBH's gravitational potential [7]. For instance, in a standard Navarro-Frenk-White (NFW) profile derived from N-body simulations, which neglect the SMBH, the energy density $\rho(r) \propto r^{-1}$ in the central region, where r represents the distance from the galaxy's center [15]. The presence of an SMBH, assuming its adiabatic growth, leads to the formation of a DM spike, with its density scaling as $\propto r^{-7/3}$ at the center and transitioning back to the NFW profile in the outer regions. However, this adiabatic formation of a spike can be mitigated by factors such as stellar interactions [16]. Furthermore, DM annihilation introduces an upper limit on the density, inversely proportional to $\langle\sigma v\rangle$, the thermally averaged cross-section times the relative velocity of DM particles, which effectively regulates the central spike into a flat core [7].

Depending on their mass and interaction channels with Standard Model particles, DM can annihilate into a spectrum of final-state particles, notably electrons and positrons in this study, which emit synchrotron radiation in magnetic fields [17]. These particles, after being produced near an SMBH, move under the influence of both gravitational and magnetic fields. We have developed a comprehensive framework, detailed in Supplemental Material, to calculate the steady-state electron-positron spectrum after propagation in the complex magnetic field environment surrounding an SMBH. This framework represents an advancement over prior spherical models of DM propagation [13, 14, 18, 19], aiming for a more astrophysically precise description.

The background magnetic field utilized for calculating the propagation of electrons and positrons is derived from a high-spin MAD model [11], which is supported by observations of the SMBH M87* by the EHT [9, 10]. As illustrated in Fig. 1, with the z -axis aligned with the BH's spin, this model reveals an azimuthal and time-averaged electron-positron density n_e concentrated primarily in the disk region, with significantly lower densities in the jet region. We utilize an axisymmetric ansatz to fit the magnetic field configurations in both the disk and jet regions, based on GRMHD simulations for the MAD. We assume that the bulk velocities of the electron/positron plasma resulting from DM annihilation align with the magnetic field lines. In the disk region, their radial components are directed towards the BH, with a magnitude scaling as $(2r_g/r)^{1/2}$, where r_g is the gravitational radius of the BH. In the jet region, we account for the rotation of the magnetic field by considering both the inertial centrifugal potential in a co-rotating frame and the gravity potential, which leads to the identification of a zero-velocity area known as the stagnation surface [20]. The initial spectra of DM-annihilated electron-positron pairs are calculated using the PPPC [17] and MadDM [21] packages.

The right panel of Fig. 1 presents an example of the

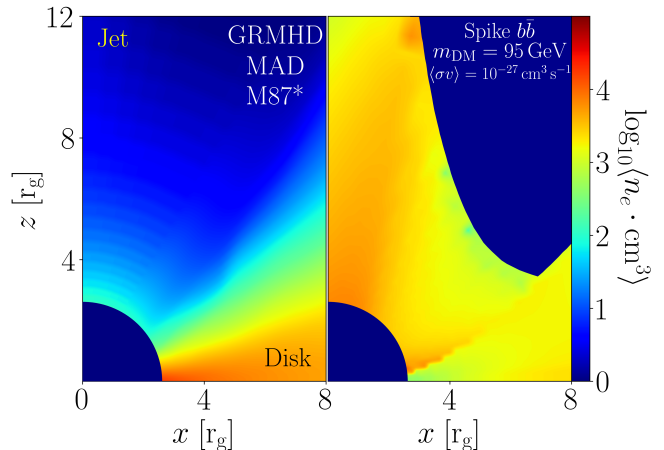


FIG. 1: Electron-positron number density n_e from an azimuthally-averaged MAD model based on GRMHD (left) versus from DM annihilation (right). The z -axis is aligned with the BH spin, adopting a dimensionless value of $a_J = 0.9375$ in the GRMHD simulation. The DM profile assumes a standard spike originating from an initial NFW profile, featuring a flat core at the center due to annihilation. In this example, the DM mass is $m_{\text{DM}} = 95 \text{ GeV}$, with the annihilation channel being $b\bar{b}$ and $\langle\sigma v\rangle = 10^{-27} \text{ cm}^3 \text{ s}^{-1}$.

resulting electron and positron density, excluding electrons from the GRMHD MAD model, where the DM mass is $m_{\text{DM}} = 95 \text{ GeV}$, with the annihilation channel being $b\bar{b}$ and $\langle\sigma v\rangle = 10^{-27} \text{ cm}^3 \text{ s}^{-1}$. The dark blue region, indicative of areas outside the stagnation surface, is not considered for conservative estimations. The densities in the jet and disk regions prove to be comparable, differing markedly from the GRMHD MAD case. This discrepancy arises because the distribution of electrons/positrons is expelled by the jet in the GRMHD scenario, whereas DM annihilation continuously supplies them within the jet cone.

III. Constraints from the EHT and ngEHT

Constraints on DM annihilation require that radiation from this process remains below the astrophysical background, positioning astrophysical radiation as a pivotal factor in determining the exclusion parameter space. We focus on the synchrotron radiation from the MAD model at 230 GHz radio frequency band. Our analysis concentrates on the synchrotron radiation emanating from the MAD model within the 230 GHz radio frequency band. By employing the RAPTOR covariant radiative transfer package [22], we generate a horizon-scale intensity (I) map for MAD outside an SMBH with $a_J = 0.9375$ and an inclination angle of $\theta_o = 163^\circ$, consistent with observations of M87*, depicted in the top left panel of Fig. 2. Subsequent application of Gaussian smearing with an ap-

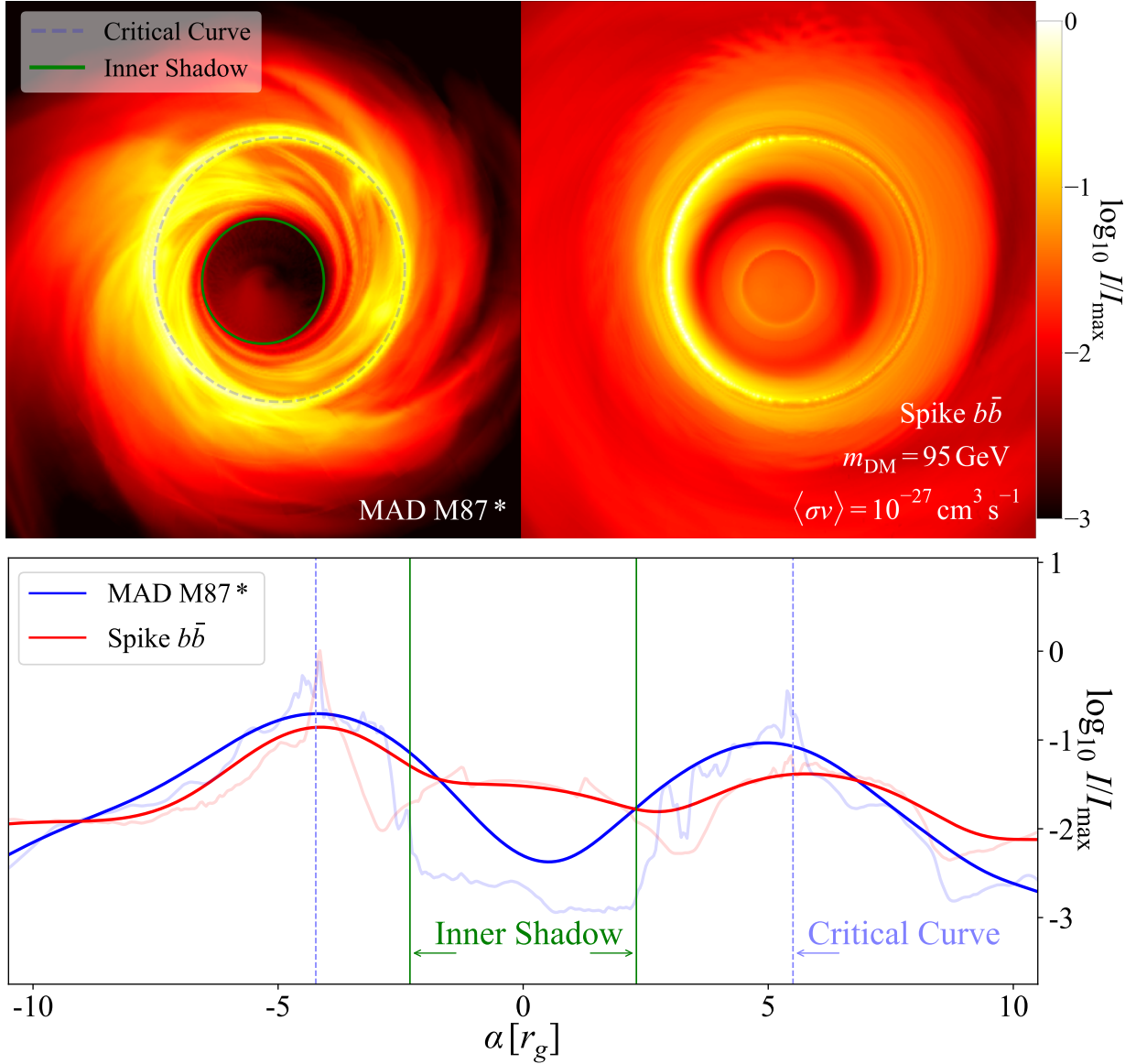


FIG. 2: Top: normalized intensity map (I/I_{\max}) in logarithmic scale comparing the MAD model from GRMHD (left) to DM annihilation (right), for the SMBH M87* with $a_J = 0.9375$ at an inclination angle of $\theta_o = 163^\circ$. Normalization is against the maximum intensity in the MAD model, I_{\max} . The critical curve and the inner shadow’s boundary are denoted by dashed and green lines, respectively. Both maps exhibit a total intensity of 0.6 Jy. Bottom: one-dimensional normalized intensity profile along the axis (α), centered on the black hole (BH) and perpendicular to the spin projection, showcasing contrasts between GRMHD MAD (blue) and DM annihilation (red) scenarios. Dark and light shades indicate the original image and its Gaussian-smoothed counterpart with an $1 r_g$ kernel, respectively.

proximately $2 r_g$ kernel to simulate the current EHT’s angular resolution yields an image that closely matches the observed data [9], with a total flux of approximately 0.6 Jy

The BH image, presented on a logarithmic scale, reveals fascinating morphological features that reflect the interplay between Kerr spacetime and the sources of emission. The dashed line in Fig. 2 delineates the critical curve, beyond which null geodesics are captured into bound orbits around the BH, creating a photon ring from

light circling multiple times [23–25]. Consequently, the intensity observed in the adjacent region results from the cumulative effect of photons undergoing multiple loops, achieving their peak in the map [26]. Within the critical curve, backward geodesics terminate at the BH horizon, known as the BH ‘shadow’ [8]. Nonetheless, this area is not completely devoid of light, as emission, proportional to electron density n_e and magnetic field strength B , reaches up to the horizon. As shown in Fig. 1 and Supplemental Material, the distribution of B slightly changes

with the polar angle, whereas n_e is predominantly found in the accretion disk, with much lower concentrations in the jet region. This distribution creates a geometrically thin emission profile mainly in the equatorial disk, leading to sharp intensity depression in the central area, identified as the ‘inner shadow’ [12]. The boundary of this inner shadow, marked in green in Fig. 2, outlines the lensed contour of the BH’s equatorial horizon.

The current EHT’s capability to detect the inner shadow is hindered by its limited dynamic range (~ 10) and angular resolution on the intensity dip. In contrast, the ngEHT is anticipated to achieve a substantial enhancement in both dynamic range (~ 1000) and angular resolution, equivalent to a Gaussian kernel of approximately $1 r_g$. This improvement holds the promise of capturing this fascinating feature and delving into the BH horizon [12]. The bottom panel of Fig. 2 displays the one-dimensional intensity distribution along an axis that crosses the BH center and is perpendicular to the projection of its spin. The use of dark and light shades serves to distinguish between the original image and the image after applying Gaussian smearing. Notably, within the inner shadow, the jet’s foreground emission is markedly lower—by two orders of magnitude—than the peak intensity, falling well within the ngEHT’s enhanced dynamic range.

The pronounced dimming within the inner shadow establishes a solid framework for testing DM annihilation. As shown in Fig. 1, the electron-positron density n_e , induced by DM annihilation, attains comparable levels in both the jet and disk regions, akin to the results observed in spherical emission models [27]. This morphology allows the DM-induced density to exceed the jet’s emission in the inner shadow area. The intensity map, derived solely from DM annihilation and presented in the top right panel of Fig. 2 with the benchmark parameters from Fig. 1, reveals a total intensity nearly matching the astrophysical emission of 0.6 Jy. In contrast, the inner shadow is significantly illuminated, lacking the expected intensity reduction. This discrepancy becomes even more evident in the bottom panel of Fig. 2, where the red line for DM annihilation markedly exceeds the expected intensity levels within the inner shadow, deviating from the astrophysical emission patterns.

In Fig. 3, we illustrate the exclusion regions derived from analyses using both the EHT and the ngEHT, targeting DM annihilation channels into $b\bar{b}$ and e^+e^- , associated with a DM spike around M87*. The constraint, illustrated in blue and based on the total intensity observed by the EHT, is derived by ensuring that the total intensity from DM annihilation does not exceed the overall astrophysical emission. Both are considered over a region extending up to $10 r_g$ from the SMBH. Conversely, the prospective morphological constraint from the ngEHT, depicted in black, imposes a stricter criterion by demanding that the local intensity resulting from DM annihilation consistently remains below the astrophysical emission within the region extending to $10 r_g$. The

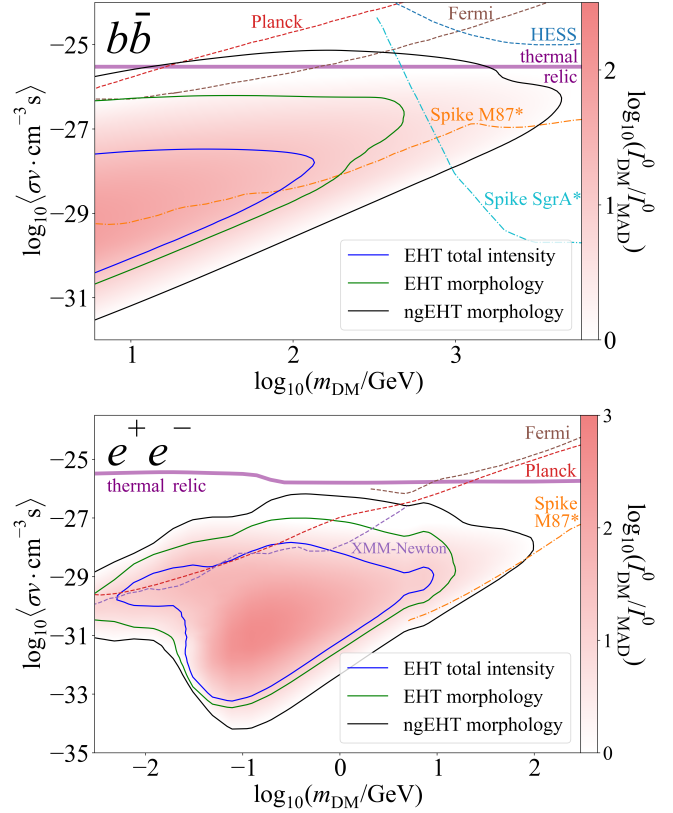


FIG. 3: Constraints on DM annihilation into $b\bar{b}$ (top panel) and e^+e^- (bottom panel) channels, incorporating total intensity constraints observed by the EHT in blue, and constraints inferred from BH image morphology by the EHT (green) and the ngEHT (black). The shaded region within the ngEHT exclusion indicates the ratio of local intensity between DM annihilation and astrophysical emissions from the MAD model in the inner shadow. The thermal relic annihilation cross-section [28] is depicted by the purple line. Previous constraints from various sources, including Planck CMB observations [29], Fermi-LAT [30], H.E.S.S. [31], AMS [32], and XMM-Newton [33, 34], as well as spike-based constraints [35, 36], are shown for comparative analysis in dashed and dot-dashed lines, respectively.

exclusion area defined by the ngEHT’s criteria markedly expands beyond that established by the EHT, underscoring the ngEHT’s increased sensitivity to the BH image’s morphology. The density within the exclusion zone represents the ratio of local intensity between DM annihilation and MAD-induced emissions in the inner shadow region. Notably, the ngEHT’s exclusion region primarily results from the enhanced visibility of the inner shadow due to DM annihilation. However, in cases with a high annihilation cross-section, the surpassing of astrophysical emission by DM annihilation becomes evident in the outer regions of the observer plane. This is due to the formation of a core of uniform density by the annihilating dark matter. The EHT’s morphological constraint, high-

lighted in green, applies criteria similar to those used by the ngEHT but includes an additional condition. Specifically, after Gaussian smearing with a $2r_g$ kernel, the local intensity resulting from DM annihilation must exceed the dynamic range threshold of 1/10. In the $b\bar{b}$ channel, the exclusion region corresponds closely to areas exhibiting the highest electron-positron densities as shown in Supplemental Material. Conversely, the exclusion criteria for the e^+e^- channel exhibit a notable turnover at around 0.1 GeV. This shift is attributed to the inadequacy of synchrotron radiation at 230 GHz for m_{DM} below 0.1 GeV.

The purple line in Fig. 3 indicates the theoretically well-motivated thermal relic annihilation cross-section [28], which the ngEHT could potentially probe for DM masses up to approximately a TeV. For context, the figure also presents previous constraints obtained from the Planck observation of the cosmic microwave background (CMB) [29], as well as constraints from the Fermi Large Area Telescope (Fermi-LAT) [30], the High Energy Stereoscopic System (H.E.S.S.) [31], the Alpha Magnetic Spectrometer Experiment (AMS) [32], and the X-ray Multi-Mirror Mission (XMM-Newton) [33, 34], depicted with dashed lines. Additionally, dot-dashed lines highlight previous constraints that are specific to a DM spike profile [35, 36]. Notably, some previous constraints derived from synchrotron radiation may lead to an overestimation of the exclusion region, attributed to the adoption of a simplified magnetic field profile [35].

IV. Discussion

The exceptional angular resolution offered by the EHT and the ngEHT not only enriches our understanding of astrophysical phenomena but also provides robust constraints on fundamental particle physics [4, 37–41]. This study illustrates how the detailed morphology of BH images, particularly the inner shadows captured by the ngEHT, can inform constraints on DM annihilation. We capitalize on the heightened DM density near SMBHs and the unique characteristics of BH images—most notably, the diminished intensity in the inner shadow area, a result of the jet’s sparse electron density. To ensure the reliability of our constraints, we have developed an advanced framework for simulating the propagation of electrons and positrons within a background fit derived from a realistic GRMHD profile. This profile is consistent with the latest intensity and polarimetric observations and represents an advancement beyond previously assumed simpler spherical accretion models [13, 14, 18, 19]. While our analysis uses M87* as a primary example, our discussions and constraints are equally applicable to another EHT focus, Sgr A*, within the Milky Way—given that observations similarly support a MAD profile around it and an almost direct line of sight [2, 42].

Looking ahead, this research aims to extensively explore DM characteristics, including an expanded range of annihilation channels, a wider spectrum of mass

scales, and exploring phenomena such as p-wave annihilation [43] and forbidden DM [44], both of which are expected to be significantly amplified in the vicinity of SMBHs. Furthermore, our analysis of the horizon-scale intensity map could be broadened to assess morphological changes at larger scales, encompassing extended jet structures and the accretion flow at greater distances from the BH. In these areas, the electron density from DM annihilation with a large cross-section decreases more slowly than the astrophysical background.

From an observational standpoint, the incorporation of linear and circular polarization intensity measurements could unveil new perspectives in differentiating between electrons and positrons [45–48]. This differentiation is crucial since astrophysical plasmas typically exhibit a significant deficit in positron populations, potentially facilitating the imposition of tighter constraints. The advent of forthcoming multi-frequency observations [49] is expected to further improve detection capabilities.

Acknowledgments

We are grateful to Richard Anantua, Marco Cirelli, Razieh Emami, Jordan Koechler, George Wong, Xiao Xue, and Yue Zhao for useful discussions. Y.C. is supported by VILLUM FONDEN (grant no. 37766), by the Danish Research Foundation, and under the European Union’s H2020 ERC Advanced Grant “Black holes: gravitational engines of discovery” grant agreement no. Gravitas-101052587, and by the European Consortium for Astroparticle Theory in the form of an Exchange Travel Grant, and by FCT (Fundação para a Ciência e Tecnologia I.P., Portugal) under project No. 2022.01324.PTDC. R.D. is supported in part by the National Key R&D Program of China (No. 2021YFC2203100). Y.M. is supported by the National Natural Science Foundation of China (Grant No. 12273022), the Shanghai Municipality orientation program of Basic Research for International Scientists (grant no. 22JC1410600), and the National Key R&D Program of China (No. 2023YFE0101200). J.S. is supported by Peking University under startup Grant No. 7101302974 and the National Natural Science Foundation of China under Grants No. 12025507, No.12150015; and is supported by the Key Research Program of Frontier Science of the Chinese Academy of Sciences (CAS) under Grants No. ZDBS-LY-7003. Y.C. and J.S. are supported by the Munich Institute for Astro-, Particle and BioPhysics (MIAPbP), which is funded by the Deutsche Forschungsgemeinschaft (DFG, German Research Foundation) under Germany’s Excellence Strategy – EXC-2094 – 390783311.

Supplemental Materials: Illuminating Black Hole Shadow with Dark Matter Annihilation

The supplemental materials provide a comprehensive procedure for calculating the electron-positron spectrum outside the black hole (BH) resulting from dark matter (DM) annihilation, as well as the intensity map derived from synchrotron radiation emitted by these electrons and positrons. Additionally, the formalism for the critical curve and the contour of the inner shadow is included. Throughout this study, we employ natural units.

I. Electron-Positron Spectrum from Dark Matter Annihilations near Supermassive Black Holes

This section examines the propagation of charged particles emerging from DM pair annihilations near supermassive BHs (SMBHs). We emphasize the significant role of electrons and positrons as primary contributors to synchrotron emission. Their propagation is analyzed in terms of energy gains from adiabatic accretion influenced by the SMBH's gravitational potential, alongside energy losses through various radiative mechanisms, culminating in a steady-state distribution in phase space.

A. Propagation of Electrons and Positrons

After being generated from DM annihilations, the flow of electrons and positrons navigates through an environment shaped by astrophysical accretion flows and the gravitational potential of the SMBH. The steady-state phase space distribution of these electrons and positrons from DM annihilation, denoted as $f_e(\vec{r}, \vec{p})$, is defined at position \vec{r} with momentum \vec{p} . This distribution adheres to the transport equation [18, 50]:

$$\nabla \cdot (\vec{v}_b f_e) + \nabla_p \cdot (\dot{\vec{p}}_{\text{adi}} f_e) + \nabla_p \cdot (\dot{\vec{p}}_{\text{rad}} f_e) + \nabla \cdot (D_{xx} \nabla f_e) + \nabla_p \cdot (D_{pp} \nabla_p f_e) = q(\vec{r}, p). \quad (\text{S1})$$

The initial terms on the left-hand side represent the advective transport of the electron-positron flow and energy acquisition through adiabatic compression, indicated by the rate of momentum change $\dot{\vec{p}}_{\text{adi}}$, where \vec{v}_b is the flow's bulk velocity. The subsequent term addresses energy depletion via assorted radiative processes, marked by the rate of momentum change $\dot{\vec{p}}_{\text{rad}}$. The concluding terms introduce spatial diffusion and diffusive reacceleration impacts, with D_{xx} and D_{pp} symbolizing the diffusion coefficients in spatial and momentum spaces, respectively. The term $q(\vec{r}, p)$ signifies the DM source function for electrons and positrons.

Considering the relativistic speeds of electrons and positrons far surpass the flow's bulk velocity \vec{v}_b , and that the DM source function $q(\vec{r}, p)$ is isotropic in momentum space—as are the momentum change processes $\dot{\vec{p}}_{\text{adi}}$ and $\dot{\vec{p}}_{\text{rad}}$, which show no directional preference under statistical mean—it is plausible to assume that f_e exhibits isotropy in momentum space. This leads to a simplification where the dependency on \vec{p} narrows down to reliance on p alone.

The rate of momentum gain from adiabatic compression is given by $\dot{p}_{\text{adi}} = -p(\nabla \cdot \vec{v}_b)/3$. Energy losses stem from various processes, including synchrotron radiation in the presence of a background magnetic field, bremsstrahlung scattering with background ions, inverse Compton scattering with background radiation, and Coulomb scattering with background electrons. These losses are collectively denoted by $\dot{p}_{\text{rad}} = \dot{p}_{\text{syn}} + \dot{p}_{\text{brem}} + \dot{p}_{\text{IC}} + \dot{p}_{\text{C}}$. Assuming typical astrophysical conditions such as a magnetic field strength of $B \sim 1$ G, a number density of background ions and thermal electrons of $\bar{n}_{\text{ion/e}} \sim 1 \text{ cm}^{-3}$, and an energy density of background radiation of $\bar{u}_r \sim 1 \text{ eV cm}^{-3}$, the estimated orders of magnitude for various rates of momentum change are [18, 51]:

$$\begin{aligned} \dot{p}_{\text{adi}} &\approx 1.03 \times 10^{-6} \text{ GeV s}^{-1} \left(\frac{p}{1 \text{ GeV}} \right) \left(\frac{r}{r_g} \right)^{-1} \left(\frac{v_b}{0.1} \right), \\ \dot{p}_{\text{syn}} &\approx -2.01 \times 10^{-7} \text{ GeV s}^{-1} \left(\frac{B}{1 \text{ G}} \right)^2 \left(\frac{p}{1 \text{ GeV}} \right)^2, \\ \dot{p}_{\text{brem}} &\approx -1.37 \times 10^{-16} \text{ GeV s}^{-1} \left(\frac{\bar{n}_{\text{ion}}}{1 \text{ cm}^{-3}} \right) \left(\frac{p}{1 \text{ GeV}} \right) \left(\ln \frac{p}{1 \text{ GeV}} + 7.94 \right), \\ \dot{p}_{\text{IC}} &\approx -1.02 \times 10^{-16} \text{ GeV s}^{-1} \left(\frac{\bar{u}_r}{1 \text{ eV cm}^{-3}} \right) \left(\frac{p}{1 \text{ GeV}} \right)^2, \\ \dot{p}_{\text{C}} &\approx -7.62 \times 10^{-18} \text{ GeV s}^{-1} \left(\frac{\bar{n}_e}{1 \text{ cm}^{-3}} \right) \left[\ln \frac{p}{1 \text{ GeV}} + \ln \frac{\bar{n}_e}{1 \text{ cm}^{-3}} + 82.3 \right], \end{aligned} \quad (\text{S2})$$

where we take the reference length to be the gravitational radius of M87*, $r_g = 3.1 \times 10^{-4} \text{ pc}$. The signs $+/-$ represent momentum gain or loss, respectively. For adiabatic compression, we have approximated $-\nabla \cdot \vec{v}_b \approx v_b/r$. It emerges

that \dot{p}_{adi} and \dot{p}_{syn} provide the most substantial contributions, while the effects of the other terms can be considered negligible in Eq. (S1).

The spatial diffusion term is quantified by the distance over which charged particles dissipate most of their energy while diffusing, denoted as $d_L \equiv (D_{xx}p/\dot{p})^{1/2}$ [18]. In the context of Bohm diffusion, where the diffusion coefficient for electrons is given by $D_{xx} = p/(3eB)$, and considering energy losses primarily due to synchrotron radiation ($\dot{p} = \dot{p}_{\text{syn}}$), the characteristic diffusion length d_L can be approximated as

$$d_L \approx 4.18 \times 10^{-4} r_g \left(\frac{B}{1\text{G}} \right)^{-3/2}, \quad (\text{S3})$$

which is significantly less than the typical propagation lengths of electrons and positrons, estimated to be on the order of r_g . In the context of Eq. (S1), the comparative significance of the spatial diffusion relative to be synchrotron radiation is approximated by the ratio d_L/r_g . Therefore, for the purpose of our analysis, the impact of spatial diffusion can be overlooked.

The diffusive reacceleration term originates from magnetic turbulence, where stochastic acceleration by Alfvén waves contributes to the additional energy gain of charged particles. Assuming the magnetic turbulence follows a power-law spectrum with index α , the momentum-diffusion coefficient behaves as $D_{pp} \sim \beta_A^2 \zeta r_L^{\alpha-2} \lambda_{\text{max}}^{1-\alpha} p^\alpha$ [52]. Here, $\beta_A \approx 1$ represents the Alfvén velocity, $\zeta \equiv \delta B^2/B^2$ denotes the ratio of turbulent to average magnetic field strength, $r_L \equiv m/(eB)$, and λ_{max} is the maximum wavelength of the Alfvén waves. The rate of momentum gain associated with this process is expressed as

$$\dot{p}_{\text{acc}} = \frac{m_e}{p^2} \frac{\partial}{\partial p} (p^2 D_{pp}) \sim m_e \beta_A^2 \zeta r_L^{\alpha-2} \lambda_{\text{max}}^{1-\alpha} p^{\alpha-1} \approx 1.52 \times 10^{-9} \text{ GeV s}^{-1} \beta_A^2 \left(\frac{\zeta}{0.1} \right) \left(\frac{10^4 r_g}{\lambda_{\text{max}}} \right) \left(\frac{p}{\text{GeV}} \right), \quad (\text{S4})$$

adopting benchmark parameters of $\alpha = 2$, $\zeta \sim 0.1$, and $\lambda_{\text{max}} \sim 10^4 r_g$. The contribution of this term, when compared to \dot{p}_{adi} and \dot{p}_{syn} within the framework of Eq. (S1), is significantly smaller and thus can be disregarded in our analysis.

Synthesizing the discussion above, we retain only the first three terms in Eq. (S1) and simplify the \vec{p} -dependence for the isotropic distribution. Consequently, Eq. (S1) can be reformulated as

$$\vec{v}_b \cdot \nabla f_e + (\dot{p}_{\text{adi}} + \dot{p}_{\text{syn}}) \frac{\partial f_e}{\partial p} = q(\vec{r}, p) - \frac{4\dot{p}_{\text{syn}} f_e}{p}, \quad (\text{S5})$$

which characterizes the evolution of the electron-positron flow along specific streamlines, defined by the bulk velocity \vec{v}_b . Given their substantial charge-to-mass ratios, electrons and positrons closely follow the magnetic field lines. As a result, at any given point along their path, the streamline direction $\hat{v}_b(\vec{r})$ aligns with the magnetic field direction, denoted as $\hat{B}(\vec{r})$.

For convenience, we define s as the distance traveled along a streamline, parameterized by $\vec{r}(s)$. This notation helps express the rate of momentum change for electrons and positrons during their journey:

$$\frac{dp}{ds} = \frac{\dot{p}_{\text{adi}} + \dot{p}_{\text{syn}}}{v_b}, \quad (\text{S6})$$

which can be integrated to obtain:

$$p - p_{\text{inj}}(s_{\text{inj}}) = \int_{s_{\text{inj}}}^{s_{\vec{r}}} ds \frac{\dot{p}_{\text{adi}} + \dot{p}_{\text{syn}}}{v_b}. \quad (\text{S7})$$

Here, $s_{\vec{r}}$ represents the location at \vec{r} . s_{inj} is a parameter moving along the streamline, marking the starting points of a specific flow in phase space originating from DM injections, to be discussed in the next subsection, and p_{inj} is the corresponding momentum of the injection.

To resolve Eq. (S5), we first express its left-hand side as df_e/ds , and then aggregate contributions from all possible flows propagating to \vec{r} :

$$f_e(\vec{r}, p) = \int_{s_{\vec{r}}}^{s_0} ds_{\text{inj}} \frac{q(s_{\text{inj}}, p_{\text{inj}}(s_{\text{inj}}))}{v_b(s_{\text{inj}})} \exp \left[\int_{s_{\vec{r}}}^{s_{\text{inj}}} ds \frac{4\dot{p}_{\text{syn}}(s, p_{\text{inj}}(s))}{p_{\text{inj}}(s) v_b(s)} \right], \quad (\text{S8})$$

where s_0 signifies the most distant injection point along a given streamline. The relationship between p_{inj} and s is determined by Eq. (S7). By incorporating Eq. (S6) into Eq. (S8), the phase space distribution function can be articulated as:

$$f_e(\vec{r}, p) = \int_{s_{\vec{r}}}^{s_0} ds_{\text{inj}} \frac{q(s_{\text{inj}}, p_{\text{inj}}(s_{\text{inj}}))}{v_b(s_{\text{inj}})} \left(\frac{p_{\text{inj}}(s_{\text{inj}})}{p} \right)^4 G(s_{\vec{r}}) G^{-1}(s_{\text{inj}}), \quad (\text{S9})$$

where G denotes a form factor satisfying:

$$\vec{v}_b \cdot \nabla G + \frac{4}{3} G \nabla \cdot \vec{v}_b = 0, \quad (\text{S10})$$

explicitly defined as:

$$G(s_{\vec{r}}) \propto \exp \left[- \int_{s_0}^{s_{\vec{r}}} \frac{4}{3} \frac{\nabla \cdot \vec{v}_b(s)}{v_b(s)} ds \right] = \exp \left[- \int_{s_0}^{s_{\vec{r}}} \frac{4}{3} \left(\nabla \cdot \hat{v}_b(s) + \frac{1}{v_b(s)} \frac{dv_b}{ds}(s) \right) ds \right]. \quad (\text{S11})$$

The term $G(s_{\vec{r}}) G^{-1}(s_{\text{inj}})$ in Eq. (S9) delineates the contraction or dilation of the volume in the configuration space as particles are translocated from their injection point $\vec{r}_{\text{inj}}(s)$ to \vec{r} along the streamline. As delineated by Eq. (S11), G encompasses two distinct elements: the first stems from the convergence or divergence of \hat{v}_b , which aligns with the magnetic field lines; the second represents how variations in bulk velocity influence particle density. In a case of spherically symmetric magnetic fields and bulk velocities akin to free-fall, it is posited that $G(s_{\vec{r}}) \propto r^{-2}$, thereby corroborating the results in Refs. [18, 50].

For the sake of simplicity, this study does not incorporate general relativistic effects within the transport equation, an approach that remains valid for larger radii where $r \gg r_g$. Given that the significant contributions to $f_e(\vec{r}, p)$ primarily originate from injections traversing the outer region—even for locations \vec{r} in proximity to the event horizon—this assumption has a minimal impact on the numerical results.

B. Dark Matter Spike Annihilation

This section delves into the DM source function $q(\vec{r}, p)$, which connects to the DM energy density $\rho(\vec{r})$ via the equation:

$$q(\vec{r}, p) = \frac{1}{4\pi p^2} \frac{\langle \sigma v \rangle \rho^2(\vec{r})}{2m_{\text{DM}}^2} \sum_i \text{BR}_i \frac{dN_{e^\pm, i}^{\text{inj}}}{dp}(p). \quad (\text{S12})$$

In this formula, m_{DM} represents the mass of the DM particles, and $\langle \sigma v \rangle$ denotes their thermally averaged cross-section times the relative velocity. The term $dN_{e^\pm, i}^{\text{inj}}/dp$ is the electron-positron (e^\pm) injection spectrum for the annihilation channel indexed by i , which has a branching ratio BR_i . For our analysis, we focus on the benchmark annihilation channels $i = b\bar{b}$ and e^+e^- , assuming 100% branching ratios for both. The injection spectra for these channels are sourced from the PPPC [17] and MadDM [21] packages, with the latter specifically applied to the e^+e^- channel for DM masses below 5 GeV.

The DM energy density profile adopts the spike density model proposed in Ref. [7] as an illustration. Our investigation specifically concerns the SMBH M87*, with a mass of $M_{\text{BH}} = 6.5 \times 10^9 M_\odot$ [1, 53], and an associated gravitational radius $r_g \equiv GM_{\text{BH}} \approx 3.1 \times 10^{-4} \text{ pc}$. We adopt the parameterization and normalization approach as outlined in Refs. [13, 35]. Beginning with a basic power-law halo profile $\rho_{\text{halo}}(r) \propto r^{-1}$, which is representative of the inner regions of an NFW profile [15], the resultant spike profile due to adiabatic accretion by the SMBH at the galactic center is described as follows:

$$\rho(\vec{r}) = \begin{cases} 0 & r < r_{\text{crit}}(\theta, a_J), \\ \rho_{\text{sat}} \equiv m_{\text{DM}} / (\langle \sigma v \rangle t_{\text{BH}}) & r_{\text{crit}}(\theta, a_J) \leq r < r_{\text{sat}}, \\ \rho_{\text{sp}}(r) \equiv \rho_0 (r/r_0)^{-\gamma_{\text{sp}}} & r_{\text{sat}} \leq r < r_{\text{sp}}, \\ \rho_{\text{halo}}(r) = \rho_0 (r_{\text{sp}}/r_0)^{-\gamma_{\text{sp}}} (r/r_{\text{sp}})^{-1} & r \geq r_{\text{sp}}. \end{cases} \quad (\text{S13})$$

Key quantities within this equation are elucidated below:

- γ_{sp} and r_{sp} represent the slope index and the extent of the spike, respectively. These parameters are influenced by the initial halo profile without the SMBH. For an NFW halo profile described by $\rho_{\text{halo}}(r) \propto r^{-1}$ [15], we adopt $\gamma_{\text{sp}} = 7/3$ and $r_{\text{sp}} = 0.001 M_{\text{BH}}^{3/2} \rho_0^{-3/2} r_0^{-7/2}$ [7], where ρ_0 and r_0 are scale factors established via the normalization condition. The total DM mass within the SMBH's sphere of influence can be inferred by jointly analyzing stellar motion [54] and the size of the photon ring [1, 53], with an associated uncertainty of about 10% M_{BH} . Accordingly, we adopt the normalization approach from Refs. [13, 35], setting $r_0 = 10^5 r_g$, which is less than r_{sp} , and determining the enclosed total DM mass to be $\Delta M_{\text{BH}} \approx 5 \times 10^8 M_\odot$. The determination of ρ_0 is guided by the relation:

$$\int_{r \leq r_0} d^3 \vec{r} \rho(\vec{r}) \approx \Delta M_{\text{BH}}. \quad (\text{S14})$$

where the integral primarily reflects contributions from larger radii, suggesting that any potential saturation at the inner region negligibly affects the normalization. Consequently, the values of ρ_0 and r_{sp} are estimated as follows:

$$\rho_0 \approx \Delta M_{\text{BH}} / (6\pi r_0^3) \approx 3.3 \times 10^4 \text{ GeV cm}^{-3} \left(\frac{\Delta M_{\text{BH}}}{5 \times 10^8 M_\odot} \right) \left(\frac{r_0}{10^5 r_g} \right)^{-3}, \quad (\text{S15})$$

$$r_{\text{sp}} \approx 4.0 \times 10^5 r_g \left(\frac{M_{\text{BH}}}{6.5 \times 10^9 M_\odot} \right)^{3/2} \left(\frac{\rho_0}{3.3 \times 10^4 \text{ GeV/cm}^3} \right)^{-3/2} \left(\frac{r_0}{10^5 r_g} \right)^{-7/2}. \quad (\text{S16})$$

- The saturation region, defined by a density $\rho_{\text{sat}} \equiv m_{\text{DM}} / (\langle \sigma v \rangle t_{\text{BH}})$, emerges as a consequence of DM annihilations [7]. Here, the age of the BH is considered to be $t_{\text{BH}} = 10^8 \text{ yr}$ [13]. The radius of this saturated region, $r_{\text{sat}} = r_0 (\rho_0 / \rho_{\text{sat}})^{1/\gamma_{\text{sp}}}$, is calculated to ensure a seamless transition in the density profile. For M87*, the calculated values are as follows:

$$\rho_{\text{sat}} \approx 3 \times 10^{13} \text{ GeV cm}^{-3} \left(\frac{m_{\text{DM}}}{10 \text{ GeV}} \right) \left(\frac{\langle \sigma v \rangle}{10^{-28} \text{ cm}^3 \text{ s}^{-1}} \right)^{-1}, \quad (\text{S17})$$

$$r_{\text{sat}} \approx 14 r_g \left(\frac{m_{\text{DM}}}{10 \text{ GeV}} \right)^{-3/7} \left(\frac{\langle \sigma v \rangle}{10^{-28} \text{ cm}^3 \text{ s}^{-1}} \right)^{3/7}. \quad (\text{S18})$$

This relationship implies that a larger cross-section correlates with an expanded saturated region. When r_{sat} falls beneath the critical radius $r_{\text{crit}}(\theta, a_J)$, distortion of DM profile due to annihilation can be considered negligible.

- $r_{\text{crit}}(\theta, a_J)$ represents the inner boundary for the density profile, uniquely affecting the profile's spherical symmetry centered around the BH with spin a_J , due to its dependency on the polar angle θ . For massive particles bound by the BH's gravitational pull, any orbit dipping below r_{crit} is destined to plunge into the BH. The analytic expression for r_{crit} can be found in Ref. [55]. Specifically, for M87* with a spin parameter $a_J = 0.9375$, r_{crit} spans from $1.5 r_g$ at the BH's equatorial plane ($\theta = \pi/2$) to $3.5 r_g$ along the polar axis ($\theta = 0$). It is noteworthy that a comprehensive general relativistic analysis would predict a denser spike profile [56–58] than the initial model [7] incorporating the cutoff at r_{crit} , underscoring our benchmark selection as a conservative approach for establishing constraints on DM annihilation.

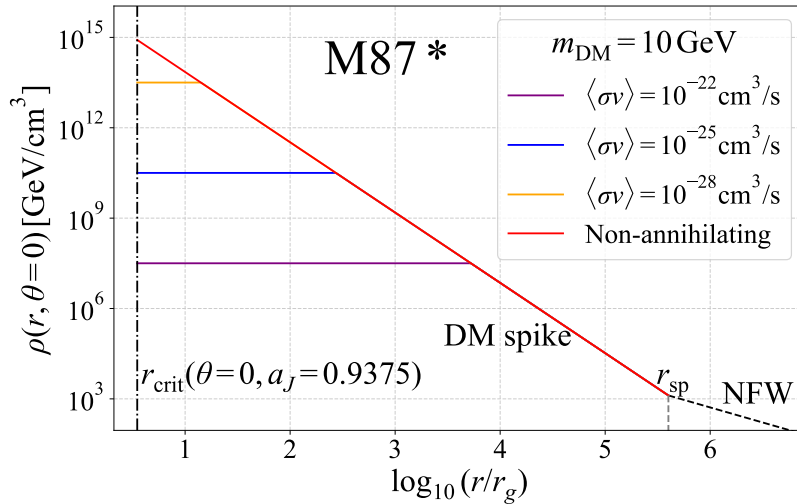


FIG. S1: DM spike density profile along the polar axis ($\theta = 0$) outside M87*, utilized in this study for different values of the thermally averaged cross-section times velocity, $\langle \sigma v \rangle$, with a fixed DM particle mass of 10 GeV. The spin of the BH that determines the cutoff radius r_{crit} is $a_J = 0.9375$.

The benchmark DM profile at the polar axis ($\theta = 0$) is shown in Fig. S1.

C. Magnetic Field Profiles from GRMHD Simulation

The magnetic field configuration incorporated into the transport equation is adapted from the results of general relativistic magnetohydrodynamic (GRMHD) simulations for the magnetically arrested disk (MAD) model [11, 59–62], as performed using the BHAC code [63, 64]. The GRMHD-generated magnetic field profile is described in cylindrical coordinates, where the z -axis aligns with the polar axis of the Kerr BH, and can be converted from the Boyer–Lindquist coordinates as $(x, \phi, z) = (r \sin \theta, \phi, r \cos \theta)$. Within this framework, the magnetic field vector is formulated as:

$$\vec{B} = B_x \hat{e}_x + B_\phi \hat{e}_\phi + B_z \hat{e}_z, \quad (\text{S19})$$

with $(\hat{e}_x, \hat{e}_\phi, \hat{e}_z)$ representing the unit vectors in the corresponding directional coordinates.

To facilitate analysis, we define dimensionless variables:

$$\tilde{r} \equiv \sqrt{\tilde{x}^2 + \tilde{z}^2} \equiv \frac{r}{r_g}, \quad \tilde{B} \equiv \frac{B}{1G}. \quad (\text{S20})$$

The GRMHD normalization ensures that the total synchrotron radiation intensity at 230 GHz matches 0.6 Jy, assuming $R_{\text{high}} = 1$ and $a_J = 0.9375$. This condition is detailed further in the subsequent section. Given the expectation for the time-averaged magnetic field to display rotational symmetry, we calculate the averaged magnetic field components over ϕ and time using data from GRMHD simulations.

Our analysis divides the magnetic field fitting process into two principal areas: the jet region, characterized by magnetic field lines intersecting the event horizon near the BH’s polar axis, and the disk region, where magnetic field lines are truncated at the BH’s equatorial plane. The fitting techniques for each region are outlined separately below:

- In the jet region, we adopt a semi-analytic ansatz based on Ref. [45] and numerically refit the parameters using GRMHD data. The ansatz implements parabolic functions centered around the polar axis given that the magnetic field configuration in this area is predominantly parabolic. A self-similarity variable, $\xi \equiv \tilde{x}^2/\tilde{z}$, is introduced to categorize magnetic field lines via magnetic flux $\Phi(\xi)$ and current $I(\xi)$. By applying Maxwell’s equations within the ideal MHD framework, the magnetic field components can be depicted as:

$$\begin{aligned} \tilde{B}_x &= \tilde{x}\Phi'/(2\pi\tilde{z}^2), \\ \tilde{B}_\phi &= I/(2\pi\tilde{x}), \\ \tilde{B}_z &= \Phi'/(2\pi\tilde{z}), \end{aligned} \quad (\text{S21})$$

with $\Phi' \equiv d\Phi/d\xi$. The current satisfies the equation $I = -2|\vec{\Omega}|\xi\Phi'$ under force-free conditions and the Ohm’s law, where $\vec{\Omega}$ denotes the angular velocity of the magnetic field line. The ansatz for $\Phi'(\xi)$ is given by:

$$\Phi'(\xi) = -c_1 \tanh(c_2 \cdot \xi) + c_3, \quad (\text{S22})$$

yielding best-fit coefficients $(c_1, c_2, c_3) = (47.3, 0.065, 70.2)$. Assuming $\vec{\Omega}$ is directed along the z -axis, its magnitude is parameterized as:

$$|\vec{\Omega}(\xi, a_J)| = d_1 + \frac{d_2}{\left(\xi + \sqrt{d_2/(\Omega_H/2 - d_1)}\right)^2}, \quad (\text{S23})$$

where $\Omega_H = a_J/\tilde{r}_H$ represents the angular velocity of the outer horizon with $\tilde{r}_H = (1 + \sqrt{1 - a_J^2})$. The ansatz in Eq. (S23) ensures that $|\vec{\Omega}(0, a_J)| = \Omega_H(a_J)/2$, a relation from GRMHD simulations [65]. The coefficients are fitted to be $(d_1, d_2) = (0.02, 36.0)$.

- In the disk region, the magnetic field lines within the $x - z$ plane adopt a hyperbolic-like configuration, consequently motivating us to use the following parameterization:

$$\frac{\tilde{B}_x}{\tilde{B}_z} = \frac{\tilde{z} \cdot K(\tilde{r})}{\tilde{x}}, \quad (\text{S24})$$

where $K(\tilde{r})$ represents the distortion near the event horizon and is modeled through a polynomial function: $K(\tilde{r}) = 1000\tilde{r}^{-4} + 100\tilde{r}^{-3} + 8\tilde{r}^{-2} + 4\tilde{r}^{-1} + 1$. This equation features two groups of hyperbolas centered on the

x -axis and z -axis, respectively; however, for our analysis focusing on the disk region, only the hyperbolas focused on the x -axis are considered. The separation between the two groups is identified as the boundary between the jet and the disk.

The overall magnitude of the magnetic field and its ϕ -component are determined by:

$$\begin{aligned}\tilde{B} &= [b_1 - b_2 \exp(b_3(\theta - \pi/4))] \tilde{r}^{-b_4}, \\ \tilde{B}_\phi &= \left[\frac{a_1}{\tilde{r} + a_2/(\cos(\theta - \pi/4) - a_3)} + a_4 \right] \tilde{B},\end{aligned}\tag{S25}$$

where $\theta = \arctan(\tilde{x}/\tilde{z})$. The coefficients determined for the best fit are:

$$\begin{aligned}(a_1, a_2, a_3, a_4) &= (4.64, 3.36, 0.20, 0.26), \\ (b_1, b_2, b_3, b_4) &= (571, 1.82, 7.14, 2.47).\end{aligned}\tag{S26}$$

As indicated, the ϕ component's proportion, \tilde{B}_ϕ/\tilde{B} , diminishes with increasing \tilde{r} . The inclusion of a constant term, a_4 , ensures that this ratio retains a specific value. The magnetic field lines exhibit a spiral pattern around the polar axis in the inner region. The selected coefficients guarantee that the \tilde{B}_ϕ fraction remains below unity within $2.5 r_g$. The field strength shows a rapid decay with distance from the BH. The coefficient b_1 parameterizes the strong magnetic field magnitude near the BH.

D. Bulk Velocity of Electron-Positron Flows

Analogous to the magnetic field profile delineated in the previous subsection, the bulk velocity \vec{v}_b exhibits distinct characteristics in the jet and disk regions, primarily due to the rotation of magnetic field lines within the jet.

Within the disk region, the gravitational influence of the SMBH directs electrons and positrons towards the BH, guiding them along the magnetic field lines. Since the Lorentz force does not affect the kinetic energy of a charged particle, the gravitational pull predominantly determines the bulk velocity's magnitude. This is represented by the radial infall velocity $v_b = (2 r_g/r)^{1/2}$. Consequently, the direction of the bulk velocity aligns with that of the magnetic field line, with its radial component consistently oriented towards the BH.

In the jet region, the magnetic field lines stretch to the event horizon, influenced by the BH rotation, which imparts a drag effect. This interaction induces rotational motion around the BH's polar axis at an angular velocity $\vec{\Omega}$. Within the frame co-rotating with the magnetic field lines, the electron-positron flow dynamics are shaped by both the inertial centrifugal potential and the BH's gravitational pull [66]. Assuming a consistent angular velocity $\vec{\Omega}$ for each magnetic field line in the jet, as derived from Eq. (S23), the bulk velocity \vec{v}_b is ascertained via energy conservation:

$$\begin{aligned}\frac{d\gamma_{v_b}}{ds} &= \hat{v}_b(\vec{r}) \cdot \left(-\frac{r_g \gamma_{v_b}}{r^3} \vec{r} - \gamma_{v_b} \vec{\Omega} \times (\vec{\Omega} \times \vec{r}) \right) \\ &= \gamma_{v_b} \left(\frac{r_g}{r^2} \frac{1 + \cos^2 \theta}{\sqrt{1 + 3 \cos^2 \theta}} - \Omega^2 r \sin^2 \theta \right),\end{aligned}\tag{S27}$$

where $\gamma_{v_b} = 1/\sqrt{1 - v_b^2}$ signifies the Lorentz factor of the bulk velocity. The stagnation surface, defined where $d\gamma_{v_b}/ds = 0$, is identified by:

$$\theta_{\text{stag}}(r) = \arccos \left(\sqrt{\frac{\Omega^2 r^3 - r_g}{\Omega^2 r^3 + r_g}} \right),\tag{S28}$$

dividing the space into regions where the bulk velocity either accelerates towards the BH (inner region) or outward towards infinity (outer region). At this surface, the bulk velocity is set to zero, $\vec{v}_b = 0$. By defining an effective potential:

$$V_{\text{eff}} = -\frac{r_g}{r} - \frac{1}{2} \Omega^2 r^2 \sin^2 \theta,\tag{S29}$$

Eq. (S27) simplifies to $d \ln \gamma_{v_b} = -dV_{\text{eff}}(r, \theta)$. Consequently, the bulk velocity magnitude inside the stagnation surface is calculated as:

$$v_b = \sqrt{1 - e^{2[V_{\text{eff}}(r, \theta) - V_{\text{eff}}(r_{\text{stag}}, \theta_{\text{stag}})]}},\tag{S30}$$

where $(r_{\text{stag}}, \theta_{\text{stag}})$ denotes the intersection of the magnetic field line, traversing through (r, θ) , with the stagnation surface.

E. Numerical Procedure and Results

We discuss the detailed procedure for calculating the electron-positron phase space, $f_e(\vec{r}, p)$, which is a solution to the propagation equation in Eq. (S5). An integral solution is provided in Eq. (S9), integrating the injection of electron/positron from DM annihilation along each streamline parameterized using $\vec{r}(s)$.

We first solve for the injected momentum, $p_{\text{inj}}(s_{\text{inj}})$, along the streamline that ultimately contributes to the momentum p in $f_e(\vec{r}, p)$. To expedite the calculation, we note the existence of an integral form of the solution for Eq. (S6), given by:

$$\frac{1}{p_{\text{inj}}(s_{\text{inj}})} = \chi(s_{\text{inj}}, s_{\vec{r}}) \left[\frac{1}{p} - \beta(s_{\text{inj}}, s_{\vec{r}}) \right], \quad (\text{S31})$$

where we introduce

$$\chi(s_{\text{inj}}, s_{\vec{r}}) \equiv \exp \left[\int_{s_{\vec{r}}}^{s_{\text{inj}}} \frac{\nabla \cdot \vec{v}_b(s')}{3v_b(s')} ds' \right] = \left(\frac{G(s_{\vec{r}})}{G(s_{\text{inj}})} \right)^{1/4}, \quad (\text{S32})$$

$$\beta(s_{\text{inj}}, s_{\vec{r}}) \equiv \frac{e^4}{36\pi^2 m_e^4} \int_{s_{\vec{r}}}^{s_{\text{inj}}} \frac{B(s')^2}{v_b(s')} \exp \left[- \int_{s_{\vec{r}}}^{s'} \frac{\nabla \cdot \vec{v}_b(s'')}{3v_b(s'')} ds'' \right] ds', \quad (\text{S33})$$

satisfying $\chi(s_{\vec{r}}, s_{\vec{r}}) = 1$ and $\beta(s_{\vec{r}}, s_{\vec{r}}) = 0$, respectively.

For each point \vec{r} , we calculate the χ and β functions along the streamline passing through it until the streamline reaches the boundary s_0 . We consider the regions for the jet and the disk as follows:

$$\begin{aligned} \text{Jet region : } r &\in [2.5, 50] r_g, \quad \theta \in [0, \frac{\pi}{2}), \\ \text{Disk region : } r &\in [2.5, 100] r_g, \quad \theta \in [\frac{\pi}{4}, \frac{\pi}{2}). \end{aligned} \quad (\text{S34})$$

Due to the existence of the stagnation surface, the upper limit in the jet region is smaller than that in the disk. The range for θ is determined by the asymptotic behavior that characterizes the boundary between the jet and disk regions, with θ approaching $\pi/2$ near the BH event horizon and $\pi/4$ at spatial infinity.

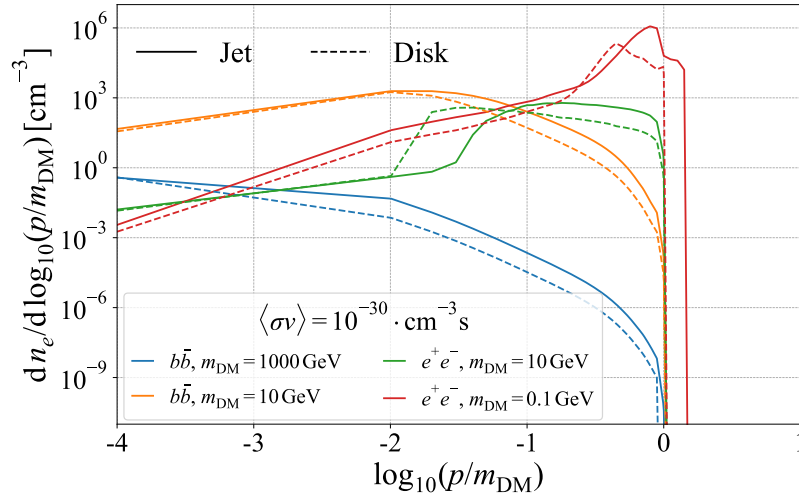


FIG. S2: Examples of the electron-positron energy spectra, $dn_e/d\log_{10} p \equiv 4\pi (\ln 10) p^3 f_e(\vec{r}, p)$ for both the $b\bar{b}$ and e^+e^- channels, at various benchmark DM masses. The spectra are depicted with solid lines for the location in the jet region $(r, \theta) = (4r_g, \pi/16)$ and with dashed lines for the point in the disk region $(r, \theta) = (4r_g, 7\pi/16)$.

Incorporating Eq. (S31) and Eq. (S12) into Eq. (S9), we obtain $f_e(\vec{r}, p)$. The range for p_{inj} is specified by the injection spectrum $dN_{e^\pm, i}^{\text{inj}}/dE(p_{\text{inj}})$, generated using the PPPC [17] and MadDM [21] packages, with the latter applied exclusively to the e^+e^- channel for DM masses below 5 GeV. Furthermore, the injection spectrum for the e^+e^- channel exhibits a sharp peak as p_{inj} approaches m_{DM} . To improve numerical precision during integration, we fit the region near the

peak with a half-Gaussian function, ensuring normalization to maintain the total number of injected e^\pm particles. Based on the given injection spectra, the range of p_{inj} is determined as follows:

$$p_{\text{inj}} \in \begin{cases} [1 \text{ keV}, m_{\text{DM}}] & \text{for } m_{\text{DM}} \in [1 \text{ MeV}, 5 \text{ GeV}), \\ [10^{-7} m_{\text{DM}}, m_{\text{DM}}] & \text{for } m_{\text{DM}} \in [5 \text{ GeV}, 6 \text{ TeV}]. \end{cases} \quad (\text{S35})$$

Consequently, the range of p is set as $p \in [1 \text{ MeV}, 10 \text{ TeV}]$, where the lower bound of p is truncated at 1 MeV to ensure that electrons and positrons remain relativistic. This broader range of p compared to p_{inj} allows for the inclusion of both acceleration and deceleration processes that electrons and positrons undergo during propagation.

In Fig. S2, we present the electron-positron energy spectra $dn_e/d\log_{10} p \equiv 4\pi (\ln 10) p^3 f_e(\vec{r}, p)$ for both the e^+e^- and $b\bar{b}$ channels, across various benchmark DM masses. We have selected spatial positions \vec{r} corresponding to two distinct points: one in the jet region $(r, \theta) = (4r_g, \pi/16)$ contributing to emissions in the inner shadow, and another in the disk region $(r, \theta) = (4r_g, 7\pi/16)$. The distribution of the electron-positron energy spectrum generally maintains the shape of the injection spectrum, although distortions and energy shifts occur due to propagation effects. Specifically, in the jet region, the adiabatic compression rate \dot{p}_{adi} can surpass the synchrotron loss rate \dot{p}_{syn} , consequently accelerating electrons and positrons to energies exceeding m_{DM} . Conversely, in the disk region, adiabatic expansion dominates, leading to energy losses that predominantly shape the propagation process and truncate the energy spectrum around $p \sim m_{\text{DM}}$.

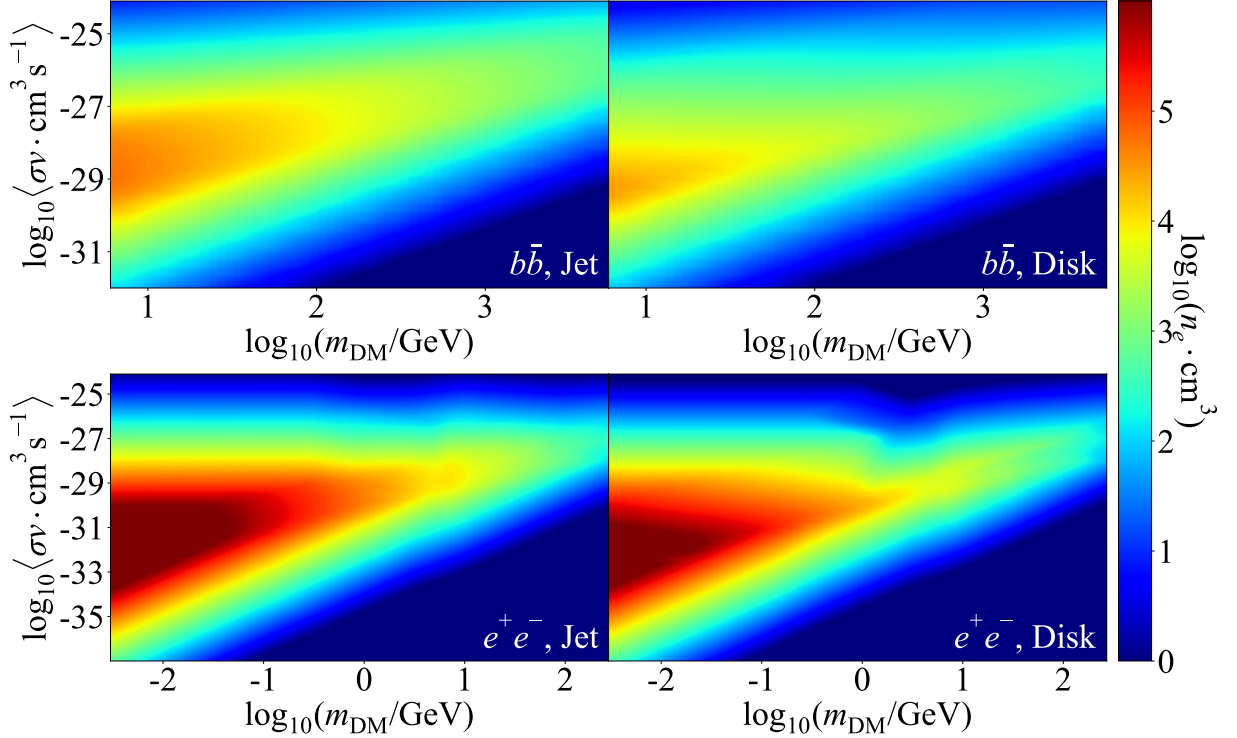


FIG. S3: The electron-positron number density, $n_e(\vec{r}) \equiv \int 4\pi p^2 f_e(\vec{r}, p) dp$, depicted across the $(m_{\text{DM}}, \langle\sigma v\rangle)$ plane for both the $b\bar{b}$ and e^+e^- channels. The spatial locations are consistent with those in Fig. S2.

In Fig. S3, we further illustrate the electron-positron number density, $n_e(\vec{r}) \equiv \int 4\pi p^2 f_e(\vec{r}, p) dp$, across the $(m_{\text{DM}}, \langle\sigma v\rangle)$ plane. The selected locations are consistent with those used in Fig. S2. For both the $b\bar{b}$ and e^+e^- channels, we observe a similar distribution pattern, which exhibits distinct characteristics in the high and low $\langle\sigma v\rangle$ regions. This delineation is attributable to the parameter space where the saturation radius of the DM profile, r_{sat} , as defined in Eq. (S18), approximates the typical propagation length scale of electrons/positrons of about $10r_g$, represented by the relation:

$$\langle\sigma v\rangle_{\text{sat}} \approx 10^{-28} \left(\frac{m_{\text{DM}}}{22 \text{ GeV}} \right) \times \left(\frac{r_{\text{sat}}}{10 r_g} \right)^{7/3} \text{ cm}^3 \text{ s}^{-1}. \quad (\text{S36})$$

The analysis leads to two key observations:

- In regions where $\langle\sigma v\rangle \geq \langle\sigma v\rangle_{\text{sat}}$, the DM density relevant for propagation saturates at $\rho(\vec{r}) = \rho_{\text{sat}} \equiv m_{\text{DM}}/(\langle\sigma v\rangle t_{\text{BH}})$. Consequently, $n_e(\vec{r}) \propto \langle\sigma v\rangle \rho_{\text{sat}}^2/m_{\text{DM}}^2$ scales as $1/\langle\sigma v\rangle$, independent of m_{DM} , which corresponds to the nearly horizontal contour line in the high $\langle\sigma v\rangle$ region depicted in Fig. S3.
- When $\langle\sigma v\rangle \ll \langle\sigma v\rangle_{\text{sat}}$, the nearby DM energy density conforms to the spike profile $\rho(\vec{r}) = \rho_0 (r/r_0)^{-\gamma_{\text{sp}}}$. Therefore, $n_e(\vec{r})$ varies as $\langle\sigma v\rangle/m_{\text{DM}}^2$, aligning with the contour slope in the low $\langle\sigma v\rangle$ region depicted in Fig. S3.

II. Covariant Radiative Transfer and Intensity Map

Following the computation of the electron and positron spectrum, $f_e(\vec{r}, p)$, we employ the covariant radiative transfer formalism [67, 68] to determine the intensity at each point on the observer plane, contrasting these results with the astrophysical background using the **RAPTOR** package [22, 69]. This section elaborates on the methodology.

To compute the flux, we initially calculate geodesics that connect the observer to the BH, utilizing the backward ray tracing method [25, 70]. Each point on the observer plane is associated with a distinct initial direction of these geodesics. The observer plane's critical curve demarcates the regions for geodesics that either propagate to infinity or terminate at the BH [23–25].

The next step involves integrating emissions along the geodesics, tracing from the BH side towards the observer. A practical approach for this integration is through the covariant radiative transfer equation [67, 68]:

$$\frac{d}{d\lambda} \left(\frac{I_\nu}{\nu^3} \right) = \frac{j_\nu}{\nu^2} - \nu \alpha_\nu \left(\frac{I_\nu}{\nu^3} \right), \quad (\text{S37})$$

defined within a local reference frame. In this equation, λ denotes the affine parameter, I_ν the intensity, j_ν the emissivity, and α_ν the absorption coefficient, with the subscript ν indicating the photon frequency in the reference frame, which is related to the observed frequency ν_0 by a redshift factor. The calculation can proceed in any frame as the quantities I_ν/ν^3 , j_ν/ν^2 , and $\nu\alpha_\nu$ are invariant under Lorentz transformation.

In practice, we select the plasma frame, where the momentum distribution of electrons/positrons at each spatial point is isotropic. The emissivity from synchrotron radiation in this frame is expressed as

$$j_\nu = \int f_e(\vec{r}, p) \eta 4\pi p^2 dp, \quad \eta = \frac{\sqrt{3}e^3 B \sin \theta_B}{8\pi^2 m_e} F\left(\frac{\nu}{\nu_c}\right), \quad F(x) \equiv x \int_x^\infty K_{5/3}(\zeta) d\zeta, \quad (\text{S38})$$

where η encapsulates the averaged angular power spectral density of synchrotron radiation at frequency ν , emitted by a single relativistic electron with momentum p orbiting in a magnetic field \vec{B} . θ_B denotes the pitch angle between \vec{B} and the photon's spatial momentum, and $K_{5/3}(\zeta)$ represents a modified Bessel function. The critical frequency, $\nu_c \equiv 3eBp^2 \sin \theta_B / (4\pi m_e^3)$, characterizes the peak of the synchrotron radiation spectrum. Similarly, the plasma frame's absorption coefficient integrates over η :

$$\alpha_\nu = -\frac{1}{\nu^2} \int \frac{df_e(\vec{r}, p)}{dp} \eta 4\pi p^2 dp. \quad (\text{S39})$$

The plasma frame is distinguished from the BH frame by a boost transformation, employing the bulk velocity of electrons/positrons, \vec{v}_b . To transform the spatial velocity into a 4-velocity, u^μ , we enforce $\vec{u} = u^0 \vec{v}_b$, ensuring it meets the normalization condition $u_\mu u^\mu = -1$. With the observed frequency ν_0 set at infinity, we determine the frequency at a given plasma frame as follows:

$$\nu = \left| \frac{1}{2\pi} g_{\mu\beta} k^\mu u^\beta \right|. \quad (\text{S40})$$

Here, $g_{\mu\beta}$ represents the Kerr metric. $k^\mu = dx^\mu/d\lambda$ represents the photon's momentum, tracing along the geodesics, normalized by fixing the affine parameter at infinity such that $k^0 = 2\pi\nu_0$, where x^μ indicates the coordinate components within the Kerr metric. In scenarios where $\vec{v}_b = 0$, the deviation from ν_0 results solely from gravitational redshift, simplifying to $\nu = \nu_0/\sqrt{|g_{00}|} = \nu_0/\sqrt{1 - 2GM_{\text{BH}}/r}$ for a non-rotating BH. Conversely, far from the BH, the Doppler shift can predominate, with $\nu = \nu_0/\sqrt{(1 + v \cos \theta_v)/(1 - v \cos \theta_v)}$, where θ_v is the pitch angle between \vec{v}_b and \vec{k} . For plasma surrounding an SMBH, both gravitational redshift and Doppler shift contribute.

We independently calculate the intensity map from a GRMHD profile of a MAD [11, 60–62] and from DM annihilation. The GRMHD profile assumes a thermal electron distribution characterized by a local temperature, $T_e(\vec{r})$.

Under this thermal distribution, the emissivity and absorption coefficients are given by:

$$j_\nu^{\text{th}} = \frac{\sqrt{3}n_e e^3 B \sin \theta_B}{8\pi m_e} \int_0^\infty F\left(\frac{\nu}{\nu_c^{\text{th}} z^2}\right) e^{-z} z^2 dz, \quad \alpha_\nu^{\text{th}} = j_\nu^{\text{th}} \frac{\exp(2\pi\nu/T_e) - 1}{4\pi\nu^3}. \quad (\text{S41})$$

In this expression, $\nu_c^{\text{th}} \equiv 3eBT_e^2 \sin \theta_B / (4\pi m_e^3)$, derived from ν_c by substituting momentum p with temperature T_e . For the DM annihilation contribution, treated as a deviation from the astrophysical background, we consider the absorption coefficient, α_ν , to originate from the GRMHD model. It is found that absorption is consistently subdominant in a MAD profile:

$$\alpha_\nu \approx 1.3 \times 10^{-4} r_g^{-1} \left(\frac{n_e}{10^4 \text{ cm}^{-3}}\right) \left(\frac{T_e}{20 m_e}\right)^{-3} \left(\frac{\nu}{230 \text{ GHz}}\right)^{-1}, \quad (\text{S42})$$

aligning with observations that favor an optically thin accretion flow at $\nu_0 = 230 \text{ GHz}$ [71–73].

Two key parameters must be defined for the GRMHD profile: the overall normalization of physical quantities and the electron temperature T_e , since only the proton temperature T_p is directly provided. The electron temperature can be inferred using the relation [22, 74]:

$$\frac{T_p}{T_e} = R_{\text{low}} \frac{1}{1 + \beta_p^2} + R_{\text{high}} \frac{\beta_p^2}{1 + \beta_p^2}, \quad (\text{S43})$$

where $\beta_p \equiv P_{\text{gas}}/P_{\text{mag}}$ represents the ratio of gas pressure to magnetic pressure, with P_{mag} being defined as $B^2/2$. Here, R_{high} and R_{low} represent the temperature ratios of protons to electrons in areas of high and low magnetic field strengths, respectively. R_{low} is set to 1 in the simulation, in accordance with Refs. [73, 75, 76]. Variations in R_{low} have been found to exert quantitatively negligible effects on the intensity distribution [59, 77].

In the maintext, we present results specifically for a high reflectivity value of $R_{\text{high}} = 1$ and a spin parameter $a_J = 0.9375$, consistent with observations by the EHT [73, 75, 76]. To ensure the robustness of our constraints, we also explore a range of these parameters, varying R_{high} from 1 to 160 and adjusting a_J down to 0.5 [78]. For each scenario, we maintain the total intensity of the BH image at 0.6 Jy, which serves to determine the normalization of the GRMHD profile alongside the electron temperature T_e . Our analysis reveals that these variations have a quantitatively minor impact, altering the intensity by less than an order of magnitude.

The exclusion region for the e^+e^- annihilation channel displays a notable shift for DM masses below GeV scales, differing significantly from the higher mass region and the $b\bar{b}$ channel, as illustrated in Fig. 3 of the maintext. Specifically, the $b\bar{b}$ channel excludes regions of highest n_e shown in Fig. S3, whereas the e^+e^- channel exhibits a distinct turning point around 0.1 GeV. This shift is attributed to a pronounced drop in the synchrotron radiation flux at 230 GHz for DM masses below 0.1 GeV. Accounting for gravitational redshift near an emission point approximately $4 r_g$ from the SMBH, the photon frequency in the plasma frame is about 300 GHz. The synchrotron radiation spectrum, for an electron or positron with momentum p , adheres to the F function as defined in Eq. (S38). This function presents a gentle slope $F \sim (\nu/\nu_c)^{1/3}$ for $\nu/\nu_c \ll 1$, transitioning to a steep decline $F \sim \exp(-\nu/\nu_c)$ for ν exceeding ν_c . The critical frequency $\nu_c \equiv 3eBp^2 \sin \theta_B / (4\pi m_e^3)$ is estimated numerically as:

$$\nu_c \approx 180 \text{ GHz} \times \left(\frac{B}{7 \text{ G}}\right) \times \left(\frac{p}{0.1 \text{ GeV}}\right)^2. \quad (\text{S44})$$

Referencing Fig. S2, the spectrum of electrons and positrons predominantly corresponds to $p \sim m_{\text{DM}}$. Thus, most synchrotron radiation emanating from the annihilation products of DM with mass below 0.1 GeV fails to contribute significantly at $\nu = 230 \text{ GHz}$.

III. Critical Curve and Inner Shadow Contour

In this section, we elucidate the equations defining the critical curve and the contour of the inner shadow, as depicted in Fig. 2, employing dimensionless notation denoted by $\tilde{\cdot}$, normalized by the gravitational radius r_g .

We commence by defining a universal coordinate system $(\tilde{\alpha}, \tilde{\beta})$ on the observer plane, where the $\tilde{\alpha}$ -axis is perpendicular to, and the $\tilde{\beta}$ -axis is parallel with, the projected spin of the BH [25, 70]. Each point on this plane corresponds to a null geodesic in Kerr spacetime, described by two conserved quantities: the energy-rescaled angular momentum $\tilde{\lambda}$ and the Carter constant $\tilde{\eta}$, expressed as [79–83]:

$$\begin{aligned} \tilde{\lambda} &= -\tilde{\alpha} \sin \theta_o, \\ \tilde{\eta} &= (\tilde{\alpha}^2 - a_J^2) \cos^2 \theta_o + \tilde{\beta}^2, \end{aligned} \quad (\text{S45})$$

with θ_o denoting the observer's inclination angle relative to the BH, which for M87* is considered to be 163° .

The critical curve demarcates the boundary on the observer plane between geodesics that terminate on the BH (inner) and those that escape to infinity (outer). It signifies the locus of bound orbits around the Kerr BH [8, 23–25, 84], maintaining a constant radius \tilde{r}_c within the range $\tilde{r}_c \in [\tilde{r}_c^-, \tilde{r}_c^+]$, where

$$\tilde{r}_c^\pm \equiv 2 \left[1 + \cos \left(\frac{2}{3} \arccos(\pm a_J) \right) \right]. \quad (\text{S46})$$

Determining the bound orbits involves identifying the double roots of the radial potential in the geodesics equation, leading to:

$$\begin{aligned} \tilde{\lambda}_c &= a_J + \frac{\tilde{r}_c}{a_J} \left[\tilde{r}_c - \frac{2\Delta(\tilde{r}_c)}{\tilde{r}_c - 1} \right], \\ \tilde{\eta}_c &= \frac{\tilde{r}_c^3}{a_J^2} \left[\frac{4\Delta(\tilde{r}_c)}{(\tilde{r}_c - 1)^2} - \tilde{r}_c \right], \end{aligned} \quad (\text{S47})$$

where $\Delta(\tilde{r}_c) = \tilde{r}_c^2 + a_J^2 - 2\tilde{r}_c$. By parameterizing \tilde{r}_c and correlating Eq. (S45) with Eq. (S47), we formulate a parametric depiction of the critical curve on the $\tilde{\alpha} - \tilde{\beta}$ plane.

The contour of the inner shadow is delineated as the lensing image of the BH's equatorial horizon, as presented in Ref. [12]. This contour becomes measurable when the emission originates from the BH's equatorial plane and reaches out to the horizon. For observers with a nearly face-on view, where $|\cos \theta_o| \approx 1$, a fitting function has been derived to accurately depict the contour on the observer's plane [12]:

$$\tilde{\rho} = \left[2\sqrt{\tilde{r}_H} + \left(1 + \frac{1}{2} \cos^2 \theta_o \right) \arctan [\sin \varphi \tan \theta_o] \right], \quad (\text{S48})$$

where $(\tilde{\rho}, \varphi)$ represents the polar coordinates on the observer's plane, linked to Cartesian coordinates through the relationship $(\tilde{\alpha}, \tilde{\beta}) = (\tilde{\rho} \cos \varphi, \tilde{\rho} \sin \varphi)$.

-
- [1] Kazunori Akiyama *et al.* (Event Horizon Telescope), “First M87 Event Horizon Telescope Results. I. The Shadow of the Supermassive Black Hole,” *Astrophys. J. Lett.* **875**, L1 (2019), [arXiv:1906.11238 \[astro-ph.GA\]](#).
 - [2] Kazunori Akiyama *et al.* (Event Horizon Telescope), “First Sagittarius A* Event Horizon Telescope Results. I. The Shadow of the Supermassive Black Hole in the Center of the Milky Way,” *Astrophys. J. Lett.* **930**, L12 (2022), [arXiv:2311.08680 \[astro-ph.HE\]](#).
 - [3] Michael D. Johnson *et al.*, “Key Science Goals for the Next-Generation Event Horizon Telescope,” *Galaxies* **11**, 61 (2023), [arXiv:2304.11188 \[astro-ph.HE\]](#).
 - [4] D. Ayzenberg *et al.*, “Fundamental Physics Opportunities with the Next-Generation Event Horizon Telescope,” (2023), [arXiv:2312.02130 \[astro-ph.HE\]](#).
 - [5] J. Silk *et al.*, *Particle Dark Matter: Observations, Models and Searches*, edited by Gianfranco Bertone (Cambridge Univ. Press, Cambridge, 2010).
 - [6] Simon Knapen, Tongyan Lin, and Kathryn M. Zurek, “Light Dark Matter: Models and Constraints,” *Phys. Rev. D* **96**, 115021 (2017), [arXiv:1709.07882 \[hep-ph\]](#).
 - [7] Paolo Gondolo and Joseph Silk, “Dark matter annihilation at the galactic center,” *Phys. Rev. Lett.* **83**, 1719–1722 (1999), [arXiv:astro-ph/9906391](#).
 - [8] Heino Falcke, Fulvio Melia, and Eric Agol, “Viewing the shadow of the black hole at the galactic center,” *Astrophys. J. Lett.* **528**, L13 (2000), [arXiv:astro-ph/9912263](#).
 - [9] Kazunori Akiyama *et al.* (Event Horizon Telescope), “First M87 Event Horizon Telescope Results. IV. Imaging the Central Supermassive Black Hole,” *Astrophys. J. Lett.* **875**, L4 (2019), [arXiv:1906.11241 \[astro-ph.GA\]](#).
 - [10] Kazunori Akiyama *et al.* (Event Horizon Telescope), “First M87 Event Horizon Telescope Results. VII. Polarization of the Ring,” *Astrophys. J. Lett.* **910**, L12 (2021), [arXiv:2105.01169 \[astro-ph.HE\]](#).
 - [11] Ramesh Narayan, Igor V. Igumenshchev, and Marek A. Abramowicz, “Magnetically arrested disk: an energetically efficient accretion flow,” *Publ. Astron. Soc. Jap.* **55**, L69 (2003), [arXiv:astro-ph/0305029](#).
 - [12] Andrew Chael, Michael D. Johnson, and Alexandru Lupasasca, “Observing the Inner Shadow of a Black Hole: A Direct View of the Event Horizon,” *Astrophys. J.* **918**, 6 (2021), [arXiv:2106.00683 \[astro-ph.HE\]](#).
 - [13] Thomas Lacroix, Mansour Karami, Avery E. Broderick, Joseph Silk, and Celine Boehm, “Unique probe of dark matter in the core of M87 with the Event Horizon Telescope,” *Phys. Rev. D* **96**, 063008 (2017), [arXiv:1611.01961 \[astro-ph.GA\]](#).
 - [14] Guan-Wen Yuan, Zhan-Fang Chen, Zhao-Qiang Shen, Wen-Qing Guo, Ran Ding, Xiaoyuan Huang, and Qiang Yuan, “Constraints on dark matter annihilation from the Event Horizon Telescope observations of M87*,” *JHEP* **04**, 018 (2022), [arXiv:2106.05901 \[hep-ph\]](#).

- [15] Julio F. Navarro, Carlos S. Frenk, and Simon D. M. White, “The Structure of cold dark matter halos,” *Astrophys. J.* **462**, 563–575 (1996), [arXiv:astro-ph/9508025](#).
- [16] Eugene Vasiliev and Maxim Zelnikov, “Dark matter dynamics in Galactic center,” *Phys. Rev. D* **78**, 083506 (2008), [arXiv:0803.0002 \[astro-ph\]](#).
- [17] Marco Cirelli, Gennaro Corcella, Andi Hektor, Gert Hutsi, Mario Kadastik, Paolo Panci, Martti Raidal, Filippo Sala, and Alessandro Strumia, “PPPC 4 DM ID: A Poor Particle Physicist Cookbook for Dark Matter Indirect Detection,” *JCAP* **03**, 051 (2011), [Erratum: *JCAP* 10, E01 (2012)], [arXiv:1012.4515 \[hep-ph\]](#).
- [18] Marco Regis and Piero Ullio, “Multi-wavelength signals of dark matter annihilations at the Galactic center,” *Phys. Rev. D* **78**, 043505 (2008), [arXiv:0802.0234 \[hep-ph\]](#).
- [19] Thomas Lacroix, Celine Boehm, and Joseph Silk, “Probing a dark matter density spike at the Galactic Center,” *Phys. Rev. D* **89**, 063534 (2014), [arXiv:1311.0139 \[astro-ph.HE\]](#).
- [20] Hung-Yi Pu, Masanori Nakamura, Kouichi Hirotani, Yosuke Mizuno, Kinwah Wu, and Keiichi Asada, “Steady General Relativistic Magnetohydrodynamic Inflow/Outflow Solution along Large-Scale Magnetic Fields that Thread a Rotating Black Hole,” *Astrophys. J.* **801**, 56 (2015), [arXiv:1501.02112 \[astro-ph.HE\]](#).
- [21] Federico Ambrogi, Chiara Arina, Mihailo Backovic, Jan Heisig, Fabio Maltoni, Luca Mantani, Olivier Mattelaer, and Gopolang Mohlabeng, “MadDM v.3.0: a Comprehensive Tool for Dark Matter Studies,” *Phys. Dark Univ.* **24**, 100249 (2019), [arXiv:1804.00044 \[hep-ph\]](#).
- [22] Thomas Bronzwaer, Jordy Davelaar, Ziri Younsi, Monika Mościbrodzka, Heino Falcke, Michael Kramer, and Luciano Rezzolla, “RAPTOR I: Time-dependent radiative transfer in arbitrary spacetimes,” *Astron. Astrophys.* **613**, A2 (2018), [arXiv:1801.10452 \[astro-ph.HE\]](#).
- [23] M. A. Podurets, “Asymptotic Behavior of the Optical Luminosity of a Star in Gravitational Collapse,” *Soviet Ast.* **8**, 868 (1965).
- [24] William L. Ames and Kip S. Thorne, “The Optical Appearance of a Star that is Collapsing Through its Gravitational Radius,” *Astrophys. J.* **151**, 659 (1968).
- [25] J.-P. Luminet, “Image of a spherical black hole with thin accretion disk,” *Astron. Astrophys.* **75**, 228–235 (1979).
- [26] Tim Johannsen and Dimitrios Psaltis, “Testing the No-Hair Theorem with Observations in the Electromagnetic Spectrum: II. Black-Hole Images,” *Astrophys. J.* **718**, 446–454 (2010), [arXiv:1005.1931 \[astro-ph.HE\]](#).
- [27] Frederic H. Vincent, Samuel E. Gralla, Alexandru Lupsasca, and Maciek Wielgus, “Images and photon ring signatures of thick disks around black holes,” *Astron. Astrophys.* **667**, A170 (2022), [arXiv:2206.12066 \[astro-ph.HE\]](#).
- [28] Gary Steigman, Basudeb Dasgupta, and John F. Beacom, “Precise Relic WIMP Abundance and its Impact on Searches for Dark Matter Annihilation,” *Phys. Rev. D* **86**, 023506 (2012), [arXiv:1204.3622 \[hep-ph\]](#).
- [29] Tracy R. Slatyer, “Indirect dark matter signatures in the cosmic dark ages. I. Generalizing the bound on s-wave dark matter annihilation from Planck results,” *Phys. Rev. D* **93**, 023527 (2016), [arXiv:1506.03811 \[hep-ph\]](#).
- [30] M. Ackermann *et al.* (Fermi-LAT), “Searching for Dark Matter Annihilation from Milky Way Dwarf Spheroidal Galaxies with Six Years of Fermi Large Area Telescope Data,” *Phys. Rev. Lett.* **115**, 231301 (2015), [arXiv:1503.02641 \[astro-ph.HE\]](#).
- [31] H. Abdallah *et al.* (H.E.S.S.), “Search for dark matter annihilations towards the inner Galactic halo from 10 years of observations with H.E.S.S.,” *Phys. Rev. Lett.* **117**, 111301 (2016), [arXiv:1607.08142 \[astro-ph.HE\]](#).
- [32] Lars Bergstrom, Torsten Bringmann, Ilias Cholis, Dan Hooper, and Christoph Weniger, “New Limits on Dark Matter Annihilation from AMS Cosmic Ray Positron Data,” *Phys. Rev. Lett.* **111**, 171101 (2013), [arXiv:1306.3983 \[astro-ph.HE\]](#).
- [33] Marco Cirelli, Nicolao Fornengo, Jordan Koechler, Elena Pinetti, and Brandon M. Roach, “Putting all the X in one basket: Updated X-ray constraints on sub-GeV Dark Matter,” *JCAP* **07**, 026 (2023), [arXiv:2303.08854 \[hep-ph\]](#).
- [34] Pedro De la Torre Luque, Shyam Balaji, and Jordan Koechler, “Importance of cosmic ray propagation on sub-GeV dark matter constraints,” (2023), [arXiv:2311.04979 \[hep-ph\]](#).
- [35] Thomas Lacroix, Céline Boehm, and Joseph Silk, “Ruling out thermal dark matter with a black hole induced spiky profile in the M87 galaxy,” *Phys. Rev. D* **92**, 043510 (2015), [arXiv:1505.00785 \[astro-ph.GA\]](#).
- [36] Shyam Balaji, Divya Sachdeva, Filippo Sala, and Joseph Silk, “Dark matter spikes around Sgr A* in γ -rays,” *JCAP* **08**, 063 (2023), [arXiv:2303.12107 \[hep-ph\]](#).
- [37] Yifan Chen, Jing Shu, Xiao Xue, Qiang Yuan, and Yue Zhao, “Probing Axions with Event Horizon Telescope Polarimetric Measurements,” *Phys. Rev. Lett.* **124**, 061102 (2020), [arXiv:1905.02213 \[hep-ph\]](#).
- [38] Guan-Wen Yuan, Zi-Qing Xia, Chengfeng Tang, Yaqi Zhao, Yi-Fu Cai, Yifan Chen, Jing Shu, and Qiang Yuan, “Testing the ALP-photon coupling with polarization measurements of Sagittarius A*,” *JCAP* **03**, 018 (2021), [arXiv:2008.13662 \[astro-ph.HE\]](#).
- [39] Yifan Chen, Yuxin Liu, Ru-Sen Lu, Yosuke Mizuno, Jing Shu, Xiao Xue, Qiang Yuan, and Yue Zhao, “Stringent axion constraints with Event Horizon Telescope polarimetric measurements of M87*,” *Nature Astron.* **6**, 592–598 (2022), [arXiv:2105.04572 \[hep-ph\]](#).
- [40] Yifan Chen, Chunlong Li, Yosuke Mizuno, Jing Shu, Xiao Xue, Qiang Yuan, Yue Zhao, and Zihan Zhou, “Birefringence tomography for axion cloud,” *JCAP* **09**, 073 (2022), [arXiv:2208.05724 \[hep-ph\]](#).
- [41] Yifan Chen, Xiao Xue, Richard Brito, and Vitor Cardoso, “Photon Ring Astrometry for Superradiant Clouds,” *Phys. Rev. Lett.* **130**, 111401 (2023), [arXiv:2211.03794 \[gr-qc\]](#).
- [42] R. Abuter *et al.* (GRAVITY), “Polarimetry and astrometry of NIR flares as event horizon scale, dynamical probes for the mass of Sgr A*,” *Astron. Astrophys.* **677**, L10 (2023), [arXiv:2307.11821 \[astro-ph.GA\]](#).
- [43] Katharena Christy, Jason Kumar, and Pearl Sandick, “Constraining p-wave dark matter annihilation with gamma-ray observations of M87,” *Phys. Rev. D* **108**, 103042 (2023), [arXiv:2305.05155 \[hep-ph\]](#).
- [44] Yu Cheng, Shao-Feng Ge, Xiao-Gang He, and Jie Sheng, “Forbidden dark matter combusted around supermassive black

- hole,” *Phys. Lett. B* **847**, 138294 (2023), arXiv:2211.05643 [hep-ph].
- [45] Richard Anantua, Razieh Emami, Abraham Loeb, and Andrew Chael, “Determining the Composition of Relativistic Jets from Polarization Maps,” *Astrophys. J.* **896**, 30 (2020), arXiv:1909.09230 [astro-ph.HE].
- [46] Razieh Emami, Richard Anantua, Andrew A. Chael, and Abraham Loeb, “Positron Effects on Polarized Images and Spectra from Jet and Accretion Flow Models of M87* and Sgr A*,” *Astrophys. J.* **923**, 272 (2021), arXiv:2101.05327 [astro-ph.HE].
- [47] Razieh Emami *et al.*, “Probing Plasma Composition with the Next Generation Event Horizon Telescope (ngEHT),” *Galaxies* **11**, 11 (2023), arXiv:2211.07306 [astro-ph.HE].
- [48] Richard Anantua, Angelo Ricarte, George Wong, Razieh Emami, Roger Blandford, Lani Oramas, Hayley West, Joaquin Duran, and Brandon Curd, “On the comparison of AGN with GRMHD simulations – II. M87,” *Mon. Not. Roy. Astron. Soc.* **528**, 735–756 (2024), arXiv:2309.05602 [astro-ph.HE].
- [49] Andrew Chael, Sara Issaoun, Dominic W. Pesce, Michael D. Johnson, Angelo Ricarte, Christian M. Fromm, and Yosuke Mizuno, “Multifrequency Black Hole Imaging for the Next-generation Event Horizon Telescope,” *Astrophys. J.* **945**, 40 (2023), arXiv:2210.12226 [astro-ph.HE].
- [50] Roberto Aloisio, Pasquale Blasi, and Angela V. Olinto, “Neutralino annihilation at the Galactic Center revisited,” *JCAP* **05**, 007 (2004), arXiv:astro-ph/0402588.
- [51] Andrew Chael, Ramesh Narayan, and Aleksander Sadowski, “Evolving Nonthermal Electrons in Simulations of Black Hole Accretion,” *Mon. Not. Roy. Astron. Soc.* **470**, 2367–2386 (2017), arXiv:1704.05092 [astro-ph.HE].
- [52] Charles D. Dermer, James A. Miller, and Hui Li, “Stochastic particle acceleration near accreting black holes,” *Astrophys. J.* **456**, 106 (1996), arXiv:astro-ph/9508069.
- [53] Kazunori Akiyama *et al.* (Event Horizon Telescope), “First M87 Event Horizon Telescope Results. VI. The Shadow and Mass of the Central Black Hole,” *Astrophys. J. Lett.* **875**, L6 (2019), arXiv:1906.11243 [astro-ph.GA].
- [54] Karl Gebhardt, Joshua Adams, Douglas Richstone, Tod R. Lauer, S. M. Faber, Kayhan Gültekin, Jeremy Murphy, and Scott Tremaine, “The black hole mass in m87 from gemini/nifs adaptive optics observations,” *The Astrophysical Journal* **729**, 119 (2011).
- [55] Shahar Hod, “Marginally bound (critical) geodesics of rapidly rotating black holes,” *Phys. Rev. D* **88**, 087502 (2013), arXiv:1707.05680 [gr-qc].
- [56] Laleh Sadeghian, Francesc Ferrer, and Clifford M. Will, “Dark matter distributions around massive black holes: A general relativistic analysis,” *Phys. Rev. D* **88**, 063522 (2013), arXiv:1305.2619 [astro-ph.GA].
- [57] Francesc Ferrer, Augusto Medeiros da Rosa, and Clifford M. Will, “Dark matter spikes in the vicinity of Kerr black holes,” *Phys. Rev. D* **96**, 083014 (2017), arXiv:1707.06302 [astro-ph.CO].
- [58] Zi-Chang Zhang and Yong Tang, “Velocity Distribution of Dark Matter Spike around Schwarzschild Black Holes and Effects on Gravitational Waves from EMRIs,” (2024), arXiv:2403.18529 [astro-ph.GA].
- [59] Yosuke Mizuno, Christian M. Fromm, Ziri Younsi, Oliver Porth, Hector Olivares, and Luciano Rezzolla, “Comparison of the ion-to-electron temperature ratio prescription: GRMHD simulations with electron thermodynamics,” *Mon. Not. Roy. Astron. Soc.* **506**, 741–758 (2021), arXiv:2106.09272 [astro-ph.HE].
- [60] Igor V. Igumenshchev, Ramesh Narayan, and Marek A. Abramowicz, “Three-dimensional mhd simulations of radiatively inefficient accretion flows,” *Astrophys. J.* **592**, 1042–1059 (2003), arXiv:astro-ph/0301402.
- [61] Jonathan C. McKinney, Alexander Tchekhovskoy, and Roger D. Blandford, “General Relativistic Magnetohydrodynamic Simulations of Magnetically Choked Accretion Flows around Black Holes,” *Mon. Not. Roy. Astron. Soc.* **423**, 3083 (2012), arXiv:1201.4163 [astro-ph.HE].
- [62] Alexander Tchekhovskoy, “Launching of active galactic nuclei jets,” *The Formation and Disruption of Black Hole Jets*, , 45–82 (2015).
- [63] Oliver Porth, Hector Olivares, Yosuke Mizuno, Ziri Younsi, Luciano Rezzolla, Monika Moscibrodzka, Heino Falcke, and Michael Kramer, “The black hole accretion code,” *Comput. Astrophys. Cosmol.* **4**, 1 (2017), arXiv:1611.09720 [gr-qc].
- [64] Hector Olivares, Oliver Porth, Jordy Davelaar, Elias R. Most, Christian M. Fromm, Yosuke Mizuno, Ziri Younsi, and Luciano Rezzolla, “Constrained transport and adaptive mesh refinement in the Black Hole Accretion Code,” *Astron. Astrophys.* **629**, A61 (2019), arXiv:1906.10795 [astro-ph.HE].
- [65] Masanori Nakamura *et al.*, “Parabolic Jets from the Spinning Black Hole in M87,” *Astrophys. J.* **868**, 146 (2018), arXiv:1810.09963 [astro-ph.HE].
- [66] Hung-Yi Pu, Kinwah Wu, Ziri Younsi, Keiichi Asada, Yosuke Mizuno, and Masanori Nakamura, “Observable Emission Features of Black Hole GRMHD Jets on Event Horizon Scales,” *Astrophys. J.* **845**, 160 (2017), arXiv:1707.07023 [astro-ph.HE].
- [67] Charles F. Gammie and Po Kin Leung, “A FORMALISM FOR COVARIANT POLARIZED RADIATIVE TRANSPORT BY RAY TRACING,” *The Astrophysical Journal* **752**, 123 (2012).
- [68] Jason Dexter, “A public code for general relativistic, polarised radiative transfer around spinning black holes,” *Mon. Not. Roy. Astron. Soc.* **462**, 115–136 (2016), arXiv:1602.03184 [astro-ph.HE].
- [69] Thomas Bronzwaer, Ziri Younsi, Jordy Davelaar, and Heino Falcke, “RAPTOR II: Polarized radiative transfer in curved spacetime,” *Astron. Astrophys.* **641**, A126 (2020), arXiv:2007.03045 [astro-ph.HE].
- [70] James M. Bardeen, William H. Press, and Saul A. Teukolsky, “Rotating black holes: Locally nonrotating frames, energy extraction, and scalar synchrotron radiation,” *Astrophys. J.* **178**, 347 (1972).
- [71] Feng Yuan and Ramesh Narayan, “Hot Accretion Flows Around Black Holes,” *Ann. Rev. Astron. Astrophys.* **52**, 529–588 (2014), arXiv:1401.0586 [astro-ph.HE].
- [72] M. A. Prieto, J. A. Fernandez-Ontiveros, S. Markoff, D. Espada, and O. Gonzalez-Martin, “The central parsecs of M87:

- jet emission and an elusive accretion disc,” *Mon. Not. Roy. Astron. Soc.* **457**, 3801–3816 (2016), [arXiv:1508.02302 \[astro-ph.GA\]](#).
- [73] EHT Collaboration et al (Event Horizon Telescope), “First M87 Event Horizon Telescope Results. V. Physical Origin of the Asymmetric Ring,” *Astrophys. J. Lett.* **875**, L5 (2019), [arXiv:1906.11242 \[astro-ph.GA\]](#).
 - [74] Monika Moscibrodzka, Heino Falcke, and Hotaka Shiokawa, “General relativistic magnetohydrodynamical simulations of the jet in M 87,” *Astron. Astrophys.* **586**, A38 (2016), [arXiv:1510.07243 \[astro-ph.HE\]](#).
 - [75] Kazunori Akiyama *et al.* (Event Horizon Telescope), “First M87 Event Horizon Telescope Results. VIII. Magnetic Field Structure near The Event Horizon,” *Astrophys. J. Lett.* **910**, L13 (2021), [arXiv:2105.01173 \[astro-ph.HE\]](#).
 - [76] Kazunori Akiyama *et al.* (Event Horizon Telescope), “First M87 Event Horizon Telescope Results. IX. Detection of Near-horizon Circular Polarization,” *Astrophys. J. Lett.* **957**, L20 (2023), [arXiv:2311.10976 \[astro-ph.HE\]](#).
 - [77] Mingyuan Zhang, Yosuke Mizuno, Christian M. Fromm, Ziri Younsi, and Alejandro Cruz-Orsorio, “Impacts of non-thermal emission on the images of black hole shadow and extended jets in two-temperature GRMHD simulations,” (2024), [arXiv:2404.04033 \[astro-ph.HE\]](#).
 - [78] Alejandro Cruz-Orsorio, Christian M. Fromm, Yosuke Mizuno, Antonios Nathanail, Ziri Younsi, Oliver Porth, Jordy Davelaar, Heino Falcke, Michael Kramer, and Luciano Rezzolla, “State-of-the-art energetic and morphological modelling of the launching site of the M87 jet,” *Nature Astron.* **6**, 103–108 (2022), [arXiv:2111.02517 \[astro-ph.HE\]](#).
 - [79] Brandon Carter, “Global structure of the Kerr family of gravitational fields,” *Phys. Rev.* **174**, 1559–1571 (1968).
 - [80] Samuel E. Gralla and Alexandru Lupsasca, “Null geodesics of the Kerr exterior,” *Phys. Rev. D* **101**, 044032 (2020), [arXiv:1910.12881 \[gr-qc\]](#).
 - [81] Samuel E. Gralla and Alexandru Lupsasca, “Lensing by Kerr Black Holes,” *Phys. Rev. D* **101**, 044031 (2020), [arXiv:1910.12873 \[gr-qc\]](#).
 - [82] Michael D. Johnson *et al.*, “Universal interferometric signatures of a black hole’s photon ring,” *Sci. Adv.* **6**, eaaz1310 (2020), [arXiv:1907.04329 \[astro-ph.IM\]](#).
 - [83] Alexandru Lupsasca, Daniel R. Mayerson, Bart Ripperda, and Seppe Staelens, “A Beginner’s Guide to Black Hole Imaging and Associated Tests of General Relativity,” (2024), [arXiv:2402.01290 \[gr-qc\]](#).
 - [84] Samuel E. Gralla, Daniel E. Holz, and Robert M. Wald, “Black Hole Shadows, Photon Rings, and Lensing Rings,” *Phys. Rev. D* **100**, 024018 (2019), [arXiv:1906.00873 \[astro-ph.HE\]](#).